



**HAL**  
open science

# Stability of ablation flows in inertial confinement fusion: optimal linear perturbations

Grégoire Varillon, Arnaud Couairon, Jean-Marie Clarisse

## ► To cite this version:

Grégoire Varillon, Arnaud Couairon, Jean-Marie Clarisse. Stability of ablation flows in inertial confinement fusion: optimal linear perturbations. 2021. hal-03147566

**HAL Id: hal-03147566**

**<https://polytechnique.hal.science/hal-03147566>**

Preprint submitted on 20 Feb 2021

**HAL** is a multi-disciplinary open access archive for the deposit and dissemination of scientific research documents, whether they are published or not. The documents may come from teaching and research institutions in France or abroad, or from public or private research centers.

L'archive ouverte pluridisciplinaire **HAL**, est destinée au dépôt et à la diffusion de documents scientifiques de niveau recherche, publiés ou non, émanant des établissements d'enseignement et de recherche français ou étrangers, des laboratoires publics ou privés.

# Stability of ablation flows in inertial confinement fusion: optimal linear perturbations

Grégoire Varillon<sup>1</sup>†, Jean-Marie Clarisse<sup>2,3</sup> and Arnaud Couairon<sup>4</sup>

<sup>1</sup>Centre Borelli, ENS Paris-Saclay, CNRS, Université Paris-Saclay, Gif-sur-Yvette, France

<sup>2</sup>CEA, DAM, DIF, F-91297 Arpajon, France

<sup>3</sup>Université Paris-Saclay, CEA, LMCE, 91680 Bruyères-le-Châtel, France

<sup>4</sup>CPHT, CNRS, École Polytechnique, Institut Polytechnique de Paris, F-91128 Palaiseau, France

(Received xx; revised xx; accepted xx)

Most amplified initial perturbations are found for an unsteady compressible ablation flow with nonlinear heat conduction that is relevant to inertial confinement fusion (ICF). The analysis is carried out for a self-similar base flow in slab symmetry which is descriptive of the subsonic heat wave bounded by a leading shock front, that is observed within the outer shell, or *ablator*, of an ICF target during the early stage, *shock transit phase*, of its implosion. Three dimensional linear perturbations as well as distortions of the flow external surface and shock front are accounted for. The optimisation is performed by means of direct-adjoint iterations. The derivation of a continuous adjoint problem follows from the Lagrange multipliers method. The physical analysis of these optimal perturbations reveals that nonmodal effects do exist in such an ablation flow and that transient growth may dominate the flow stability until the end of the shock transit phase, even at short wavelengths which are held as innocuous from the classical standpoint of the ablative RichtmyerMeshkov instability. Perturbations are not only amplified in the ablation front, but in the whole flow which is found to be especially sensitive to perturbations in the compression region. This fact points out ablator bulk inhomogeneities as the most detrimental defects regarding the shock transit phase of an ICF implosion.

**Key words:** Authors should not enter keywords on the manuscript, as these must be chosen by the author during the online submission process and will then be added during the typesetting process (see <http://journals.cambridge.org/data/relatedlink/jfm-keywords.pdf> for the full list)

---

## 1. Introduction

Inertial confinement fusion (ICF) has been thought in the 1950s as a way to produce the smallest possible nuclear fusion explosion, i.e. thermonuclear fusion at the scale of the laboratory (Lindl 1995). Reaching the ignition of thermonuclear reactions in the laboratory is a turning point in applied sciences for energy production and national security, as well as in basic science. Thermonuclear fusion sets off when the energy released

† Email address for correspondence: gregoire.varillon@gmail.com

by fusion reactions induces self-sustained combustion in the rest of the fuel. This ignition criterion requires to bring the fuel at high temperature and areal mass —  $10^7\text{K}$  and  $0.5\text{ g/cm}^2$  — and to maintain it in a rather spherical shape for a sufficiently long time — a few picoseconds (Atzeni & Meyer-ter-Vehn 2004). This challenge is accomplished by imploding at high velocities a spherical shell of millimetric size filled with thermonuclear fuel (a mixture of deuterium and tritium in the simplest case). During the implosion, the inertia of the shell confines the fuel while its temperature and density increase. If the implosion is sufficiently strong and symmetrical, the nuclear reactions ignite in a small volume at the center of the fuel — the *hot spot* — and then propagate to the rest of the fuel.

Inertial confinement fusion became possible with the advent of lasers, and then high energy lasers, which are capable of reaching energy densities compatible with ignition. Such lasers are used to produce an intense incident x-rays flux on the target — the containment shell filled with the fuel — that produces an *ablation wave*: a subsonic heat front preceded by a forerunning shock front (Pakula & Sigel 1985) propagating inward through the external layer of the target — the *ablator*. The ablated material expands outward as a hot plasma, resulting in an ablation pressure that sets the target into an inward converging motion (spherical rocket effect). This *shock transit phase*, i.e. when the leading shock front is travelling between the surface of energy deposition and the inner ablator surface, is depicted on figure 1. However, this compression process is subject to hydrodynamic instabilities. Indeed, the ablation pressure applies in a strongly stratified region called the *ablation layer* or *ablation front*. In the reference frame moving with the ablation front, the hot and light expanding plasma pushes the cold and heavier unablated part of the ablator. Such a configuration is unstable regarding the Rayleigh–Taylor instability. Therefore, any small perturbation of the ablation front strongly develops into spikes and bubbles as seen in the case of the classical Rayleigh–Taylor instability. These deformations degrade the symmetry of the implosion, eventually leading to mixing of the ablator material with the fuel, breaching of the confinement by breaking through the ablator, thus preventing ignition. Although numerous works have been devoted to the subject, hydrodynamic instabilities still represent a major obstacle to overcome in the view of reaching ignition (Lindl *et al.* 2014; Haines *et al.* 2019; Clark *et al.* 2019; Tommasini *et al.* 2020).

The vast majority of hydrodynamic stability analyses of ICF ablation flows have adopted a simplified modelling consisting of the equations of motion for a compressible inviscid fluid (or Euler equations) with nonlinear heat conduction. However, progress towards analytical or semi-analytical models could only be made upon using additional simplifying assumptions: e.g. flow steadiness, isobaric approximation, discontinuous ablation front, unbounded flow regions, isothermal expansion of the ablated fluid, etc. From the early description of the ablation front as a rippled surface discontinuity (Bodner 1974; Kull & Anisimov 1986), Kull & Anisimov (1986), Kull (1989) and Sanz (1996) improved the modelling by using a continuous description of the ablation front. These models have led to analytical expressions of growth rate for ablation front ripples under the form of the classical Rayleigh–Taylor growth rate (Chandrasekhar 1961) with more or less sophisticated corrective terms. Stabilizing physical mechanisms at stake have been identified as the mass flowing through the ablation layer, the dynamical overpressure and heat conduction (Goncharov *et al.* 1996).

However, the ablation layer cannot be considered in actual ICF configurations as a discontinuity — or even a strongly stratified region — between two semi-infinite slabs. The influence of the surface of energy deposition (downstream), of the forerunning shock front (upstream), at finite distances, and of travelling waves between these flow

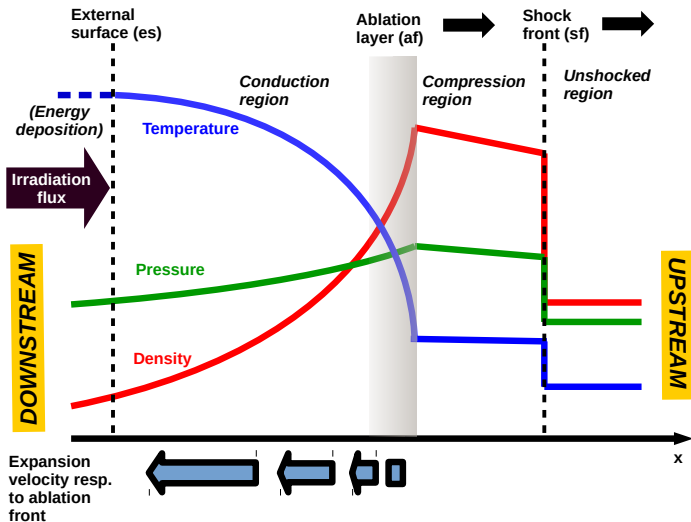


FIGURE 1. Schematic side profile of an ablation wave typical of the shock-transit phase of an ICF implosion.

‘interfaces’ must be taken into account (see figure 1). Such *confinement effects* are especially important during the shock-transit phase of a target implosion where the distances between these interfaces may be much smaller than perturbation transverse wavelengths. Three typical configurations of perturbations have been considered:

(i) The ‘ablative Richtmyer–Meshkov’ (ARM) instability (Goncharov 1999; Aglitskiy *et al.* 2010) corresponding to a uniform incident heat flux on an ablator with surface roughness: the ablative pressure at a corrugated ablation front produces a distorted shock front. A key parameter is the characteristic size of the conduction region  $l_{\text{cond}}$  (figure 2), between the ablation layer and the surface of energy deposition. Within the isobaric approximation of stationary laser-driven ablation flows, Goncharov *et al.* (2006) find that ablation front modes localized in the conduction region (i.e. of wavelength smaller than  $l_{\text{cond}}$ ) oscillate and are stabilized by a dynamical overpressure resulting from thermal conduction while the longer wavelengths are not stabilized and grow as a result of Richtmyer–Meshkov and Darrieus–Landau mechanisms, hence the following stability criterion

$$l_{\text{cond}} \geq \lambda_{\perp} \quad : \quad \text{damped oscillations,} \quad (1.1a)$$

$$l_{\text{cond}} \leq \lambda_{\perp} \quad : \quad \text{amplification.} \quad (1.1b)$$

(ii) The ‘laser imprint’ or more generally ‘illumination asymmetry’ (IA) configuration (Velikovich *et al.* 1998; Goncharov *et al.* 2000) where an ablator without roughness is illuminated by an inhomogeneous incident heat flux. This configuration leads to the same stability criterion as the ARM instability (1.1).

The ARM instability and IA configuration were long thought as being the most detrimental perturbation sources. Therefore intensive efforts were spent on surface finish requirements for fusion targets.

(iii) Bulk ablator inhomogeneities: the material of the ablator contains some inhomogeneities. This last configuration has gained recent attention after experiments (Smalyuk *et al.* 2015; Haan *et al.* 2015; Ali *et al.* 2018) exhibited that material inhomogeneities could be a major source of perturbations.

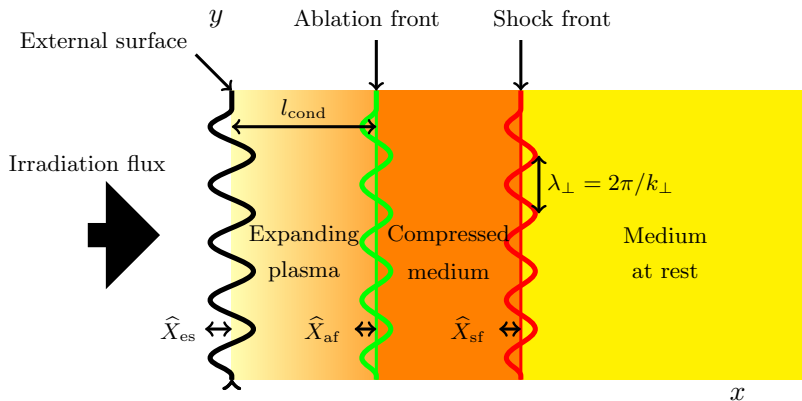


FIGURE 2. Schematic view of perturbed remarkable surfaces in a planar ablation wave. The length of the conduction region is denoted  $l_{\text{cond}}$ , and  $\hat{X}_a$ ,  $a=es, af$  or  $sf$ , denote the Fourier coefficients of the deformation of, respectively, the external surface, ablation front and shock front, of transverse wavenumber  $k_{\perp}$ .

The ARM and IA configurations led to analytical and semi-analytical models that have undoubtedly helped in getting a better understanding of ablation flows and of their instabilities. However, their results suffer from diverse limitations, among which:

- (i) Overly restrictive modelling assumptions. Compressibility effects are rarely and never fully taken into account. Actual base flow stratification and unsteadiness are ignored.
- (ii) Exclusive use of modal stability analysis. Stability results are deduced from the least stable eigensolutions, omitting possible transient growth phenomena proper to non-normal operators.
- (iii) Finally, most of the above mentioned models describe laser driven ablation and none have been dedicated to the stability of x-ray driven ablation flows.

The first limitation comes from the fact that the low-Mach number criteria are only satisfied in the close vicinity of the ablation layer, but not at other locations, especially for external heat-flux in the range of ICF-like implosions (Boudesocque-Dubois *et al.* 2008; Clarisse *et al.* 2018). This and other restrictive flow assumptions such as steadiness, isothermal expansion, etc., on which all of the above-mentioned models rely are unnecessary when considering self-similar ablation flows. Self-similar ablation flows follow from the work of Marshak (1958) (cf. also Reinicke & Meyer-ter-Vehn 1991). Self-similarity follows from Euler equations with nonlinear heat conduction upon the assumption that the incident heat-flux and pressure are growing as particular powers of time. Self-similar solutions, actually computed in (Boudesocque-Dubois 2000; Boudesocque-Dubois *et al.* 2008; Abéguilé *et al.* 2006; Clarisse *et al.* 2018), describe accurately the whole flow structure of the ablation wave, from the forerunning shock front to the external surface (see figure 1), and stand out from standard models by an exact description of the hydrodynamics. Moreover, realistic ICF flow variables profiles have been found to be close to self-similar solutions (cf. Velikovich *et al.* 1998; Boudesocque-Dubois *et al.* 2008, figure 1). When applied to the computation of linear perturbations, this approach furnishes the perturbation field in the whole extent of the ablation wave (Abéguilé *et al.* 2006; Lombard *et al.* 2008; Clarisse *et al.* 2008, 2016), and not only the shock front and ablation front deformations, as most of standard models do. These computations have also stressed the importance of short time — and potentially transient

— behaviour to the stability of ICF-like ablation flows, which leads us to the second limitation.

Because they rely on *normal mode* analyses, the standard models of ablation front instabilities previously mentioned omit potential transient growth phenomena and early-time perturbation dynamics. Corresponding stability results are valid only for asymptotically long times. Moreover, these standard models have neglected the influence of the base flow dynamics on perturbation evolution. However, using the approach of self-similar ablation waves indicates that the dynamics of the base flow influences the growth rate of perturbations: the inherent flow stretching results in an algebraic, rather than linear, growth in time for long wavelengths (1.1b) and a modification of criterion (1.1) (Abéguilé *et al.* 2006; Clarisse *et al.* 2008). Secondly, the duration of the shock transit phase is limited in time, so that results valid at asymptotically long times do not necessarily apply. There are no a priori time scale separation between the base flow, perturbation dynamics and the shock transit phase duration. Finally, the normal mode analysis does not consider interaction between eigensolutions of the flow. In particular, two individually decaying eigensolutions may interact and transiently amplify perturbations, also called *non-modal effects* (Schmid & Henningson 2001). Although such transient behaviour can amplify perturbations by several orders of magnitude, they are unpredictable by a normal mode analysis. One consequence of non-modal effects is a possible earlier transition to nonlinear behaviour than predicted by a normal mode analysis, and more generally an underestimation of perturbation amplitude.

Concurrently to stability analyses using simplified physical modellings, some ICF simulation codes trying to be as realistic as possible are routinely used to compute the amplifications of some initial perturbations. Although more accurate models are embedded in ICF simulation codes, this approach consists in computing solutions to an initial and boundary value problem (IBVP) for selected initial and/or boundary perturbations. Such computations performed for specific initial conditions are not sufficient for obtaining general stability results. Yet, these ICF simulation codes have been developed in the purpose of designing ICF targets for fusion or dedicated experiments. Due to the multiplicity of perturbation sources, experiments and ICF simulations have often focused on studying a specific source of perturbation (e.g. surface defects or internal density inhomogeneities) for given wavelengths. In dedicated experiments, an initial perturbation is artificially introduced in the shell to control its shape and size. In such cases ICF code simulations have been found in good agreement with experiments (Raman *et al.* 2014; Peterson *et al.* 2015). However, implosion simulations of ‘native roughness’ shells designed to achieve ignition still fail to produce satisfactory agreements with experiments (Raman *et al.* 2014; Smalyuk *et al.* 2017). For such shells, initial perturbations, individually considered as acceptable regarding the implosion process, may interact and lead to an amplification level not predicted by experiments and simulations. Additionally, some sources of perturbations not considered in experiments and simulations have turned out to be significant (Haan *et al.* 2015; Smalyuk *et al.* 2017; Ali *et al.* 2018). It appears that current limitations of studies on ICF implosion instabilities come predominantly from the under-appreciation of sources of perturbations (Clark *et al.* 2019, Sec. V). Non-modal effects fall in this category of ‘unappreciated effects’. Hoping to remedy to such limitations by sampling the entire range of admissible initial conditions and terminal times by a sufficiently large number of amplification computations is simply unrealistic. Sensitivity analysis regarding initial conditions has never been performed for ICF implosion flows. Non-modal analysis is able to face the challenge of the multiplicity of perturbation sources: *not missing out the most detrimental initial perturbations*.

Clarisse *et al.* (2016) called for an analysis of short-time perturbation dynamics during

the shock transit phase. Recently, Varillon *et al.* (2021) have revealed local non-modal instantaneous growths of perturbations at small scales in a self-similar ablation wave representative of ICF implosions. It has also been noticed that the non-modal behaviour of thermoacoustic instabilities — involving the same basic mechanisms as ablation flow instabilities — is favoured in accelerated flows (Nicoud *et al.* 2007) or in flows with complex boundary conditions (Wieczorek *et al.* 2011). Ablation flows present these particularities owing to pressure gradients and deformed external surface and shock front.

Up to now, short-term perturbation dynamics in ICF ablation flows have never been investigated and the present work aims at changing this fact by performing the first non-modal linear analysis of an ablation flow. This analysis is carried out in the context of the shock transit phase of an ICF target implosion since the possible occurrence of rapid transient growth of perturbations during this phase could significantly change the current understanding of hydrodynamic instabilities in ICF implosions and the methods that are required for their prediction.

The rest of the article is structured as follows. Modeling choices for ablation flows are exposed (Sec. 2), with the IBVP for linear perturbations (Sec. 2.3). Optimal initial perturbations are found thanks to an optimisation method exposed in Sec. 3. We have recourse to the use of an adjoint problem (Sec. 3.2) derived with the method of the Lagrange multipliers (Sec. 3.1). Optimal initial perturbation are presented and analysed in Sec. 4 for various parameters. These results are then discussed (Sec. 5) before a summary and some perspectives given in the conclusion (Sec. 6).

## 2. Modelling

Hydrodynamics of ICF ablation flows is classically described thanks to the equations of radiation hydrodynamics (Mihalas & Mihalas 1984). This owes to the following facts:

- the temperature within the portion of the ablator that is set into motion — above many thousand degrees Kelvin (Lindl *et al.* 2004) — indicates that the medium forms a plasma and that radiative transport cannot be neglected,
- the radiative temperature remains below a few million degrees Kelvin, so that radiative pressure and energy are negligible compared to their material counterparts,
- effects of radiative energy diffusion dominate those of viscosity and thermal conduction,
- the ablator is chosen to be opaque toward the incoming irradiation in order to be set into motion. It means that during the shock transit phase, the mean free path of photons in the cold and heavy part of the ablator is small compared to the characteristic size of the ablation wave and local gradient lengths. Therefore radiative transport is approximated by radiation heat conduction (Zel'dovich & Raizer 1967, §II.10), i.e. the radiative flux is proportional to the radiation energy gradient

$$\varphi = -\kappa(\rho, T)\nabla T^4, \quad (2.1)$$

where  $\kappa$  is the radiative heat conductivity. Radiation heat conduction is not strictly valid in the low density expansion region that is transparent to the incident radiation.

The flow dependent variables thus comprise the fluid density  $\rho$ , velocity  $\mathbf{v}$ , pressure  $p$  and temperature  $T$ . In a Cartesian coordinate system ( $O, x, y, z$ ), equations of motion in

an Eulerian description write (Hirsch 1988)

$$\partial_t \rho + \nabla(\rho \mathbf{v}) = 0, \quad (2.2a)$$

$$\partial_t(\rho \mathbf{v}) + \nabla \cdot (\rho \mathbf{v} \otimes \mathbf{v} + p\mathbb{I}) = \mathbf{0}, \quad (2.2b)$$

$$\partial_t(\rho e) + \nabla \cdot (\rho v e + \boldsymbol{\varphi} + p\mathbf{v}) = 0, \quad (2.2c)$$

with the specific total energy

$$e = \varepsilon + \mathbf{v}^2/2. \quad (2.2d)$$

The configurations of self-similar solutions correspond to the one dimensional flow — along the  $x$ -axis — of a semi-infinite slab initially at rest and of uniform finite density, for a nonlinear heat conduction of the kind  $\boldsymbol{\varphi} = -\kappa_0 \rho^{-\mu} T^\nu \nabla T$ , with  $\nu > 0$  and  $\mu \geq 0$ , and for a polytropic gas obeying the equation of state

$$\varepsilon = \frac{RT}{\gamma - 1}, \quad p = \rho RT,$$

with  $\gamma$  the adiabatic gas exponent and  $\varepsilon$  the specific internal energy. Such a flow is conveniently described in the Lagrangian coordinate  $m$ , such that  $dm = \rho dx$ . Dimensionless evolution equations come as (Boudesocque-Dubois *et al.* 2008)

$$\partial_t \left( \frac{1}{\rho} \right) - \partial_m \bar{v}_x = 0, \quad (2.3a)$$

$$\partial_t \bar{v}_x + \partial_m \bar{p} = 0, \quad (2.3b)$$

$$\partial_t (C_v \bar{T} + \bar{v}_x^2/2) + \partial_m (\bar{p} \bar{v}_x + \bar{\varphi}_x) = 0, \quad (2.3c)$$

with  $C_v = 1/(\gamma - 1)$  and  $v_x$  and  $\varphi_x$  the longitudinal components of  $\mathbf{v}$  and  $\boldsymbol{\varphi}$ , respectively. Dimensionless dependent variables  $\bar{f}$  are functions of  $(m, t)$  corresponding to the dependent variables  $f = \rho, v_x, p, T$  and  $\varphi_x$ . Dimensionless longitudinal heat flux and equation of state read

$$\bar{p} = \bar{\rho} \bar{T} \quad \text{and} \quad \bar{\varphi}_x = -\bar{\rho}^{-\mu} \bar{T}^\nu \bar{\rho} \partial_m \bar{T}. \quad (2.4)$$

### 2.1. Self-similar ablation waves

Self-similar solutions to (2.3) arise for external heat flux and pressure of the form (Boudesocque-Dubois *et al.* 2008)

$$\bar{p}(0, t) = \mathcal{B}_p t^{2\alpha-2}, \quad \bar{\varphi}(0, t) = \mathcal{B}_\varphi t^{3\alpha-3}, \quad \alpha = (2\nu - 1)/(2\nu - 2) \quad (2.5)$$

with  $\mathcal{B}_p$  and  $\mathcal{B}_\varphi$  some constants, and initial conditions

$$(\bar{\rho}, \bar{v}_x, \bar{T})(m, 0) = (1, 0, 0) \quad \text{for } m \geq 0. \quad (2.6)$$

These solutions depend on a single reduced variable  $\xi = m/t^\alpha$ . Dimensionless dependent variables  $\bar{\rho}, \bar{v}_x, \bar{T}, \bar{p}$  and  $\bar{\varphi}_x$ , corresponding to this set of solutions, are related to the reduced variables  $\bar{\mathbf{U}} = (\bar{G} \quad \bar{V}_x \quad \bar{\Theta} \quad \bar{\Phi})^\top$  and  $\bar{P}$  through the relations

$$\bar{\rho}(m, t) = \bar{G}(\xi), \quad \bar{v}_x(m, t) = t^{\alpha-1} \bar{V}_x(\xi), \quad \bar{T}(m, t) = t^{2(\alpha-1)} \bar{\Theta}(\xi), \quad (2.7a)$$

$$\bar{p}(m, t) = t^{2(\alpha-1)} \bar{P}(\xi), \quad \bar{\varphi}_x(m, t) = t^{3(\alpha-1)} \bar{\Phi}(\xi). \quad (2.7b)$$

The reduced variables  $\bar{\mathbf{U}}$  are solutions to a nonlinear ordinary differential equation

$$d_\xi \bar{\mathbf{U}} = \mathcal{F}(\xi, \bar{\mathbf{U}}), \quad (2.8)$$

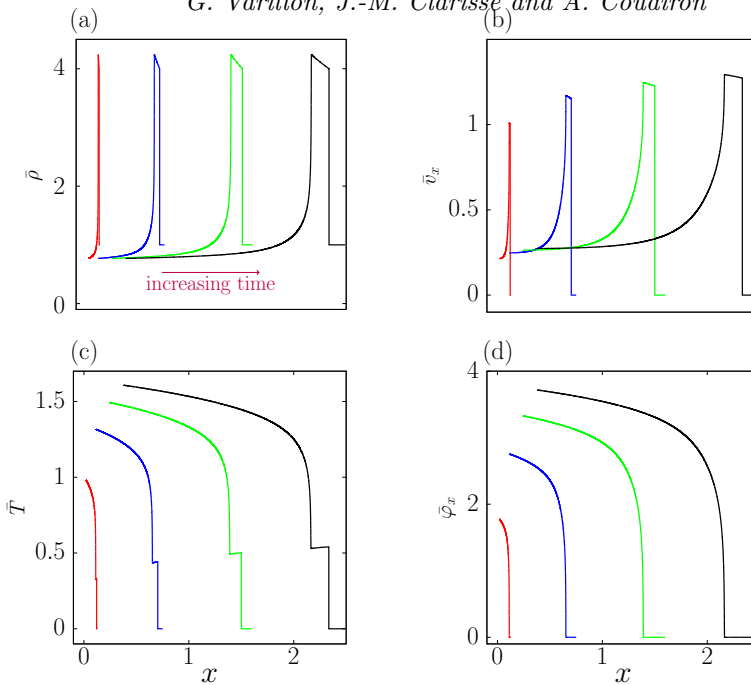


FIGURE 3. Variables in the coordinate  $x$  at increasing times for the base flow defined in table 1: (a) density, (b) longitudinal velocity, (c) temperature and (d) longitudinal heat-flux.

(cf. Boudesocque-Dubois *et al.*, 2008, Eq. 2.18 for the definition of the function  $\mathcal{F}$ ). The reduced variables satisfy the dimensionless equation of state

$$\bar{P} = \bar{G}\bar{\Theta}, \quad (2.9)$$

and the nonlinear heat flux is expressed as a function of density, temperature and its first gradient

$$\bar{\Phi} = \Psi(\bar{G}, \bar{\Theta}, \bar{G}d_\xi\bar{\Theta}), \quad \text{with } \Psi(G, \Theta, \Theta') = -G^{-\mu}\Theta^\nu\Theta'. \quad (2.10)$$

Initial and boundary conditions (2.5),(2.6) become

$$\bar{\Phi}(0) = \mathcal{B}_\varphi, \quad \bar{P}(0) = \mathcal{B}_p, \quad (2.11a)$$

$$(\bar{G}, \bar{V}_x, \bar{\Theta}) = (1, 0, 0) \quad \text{for } \xi \rightarrow \infty. \quad (2.11b)$$

For sufficiently low values of the incident heat flux, the heated fluid region may be considered to be bounded by a non-isothermal shock-wave discontinuity (Marshak 1958) propagating in the fluid at rest. This discontinuity is located at  $\xi_{\text{sf}}$ , which depends on  $\mathcal{B}_p$  and  $\mathcal{B}_\varphi$  (Boudesocque-Dubois *et al.* 2008). Under this approximation, boundary conditions at  $\xi \rightarrow \infty$  (2.11b) may be replaced by a condition at  $\xi_{\text{sf}}^-$  following from Rankine–Hugoniot jump relations between  $\bar{\mathbf{U}}(\xi_{\text{sf}}^+)$  and  $\bar{\mathbf{U}}(\xi_{\text{sf}}^-)$ , with  $\bar{\Phi}(\xi_{\text{sf}}^+) = 0$  (Boudesocque-Dubois *et al.* 2008, App. A).

## 2.2. Base flow

In the present work we consider a self-similar ablation wave pictured in figure 3 and whose characteristic parameters are described in table 1. The expansion velocity of the plasma with respect to the ablation front is quasi-sonic. Due to the self-similarity, the

---

$\gamma$	$(\mu, \nu)$	$(\mathcal{B}_\varphi, \mathcal{B}_p)$	$(\xi_{\text{af}}, \xi_{\text{sf}})$	$L_{\text{cond}}$	$\min \frac{L_{\nabla T}}{L_{\text{tot}}}$	$M_s _{\xi_{\text{af}}}$	$\max M_T$	$Fr _{\xi_{\text{af}}}$
5/3	(2, 13/2)	(3.33, 1.15)	(1.06, 1.5)	1.15	$4.0 \cdot 10^{-3}$	0.32	1.05	12.2

---

TABLE 1. Characteristic parameters of the base flow considered in the present work: adiabatic gas exponent ( $\gamma$ ), heat conduction exponents ( $\mu, \nu$ ) for the fully ionized gas model of Kramers (Zel'dovich & Raizer 1967), values of the boundary parameters ( $\mathcal{B}_\varphi, \mathcal{B}_p$ ), reduced abscissa of the ablation front  $\xi_{\text{af}}$  and shock front  $\xi_{\text{sf}}$ , size of the conduction region at  $t = 1$  ( $L_{\text{cond}}$ ), stiffness of the ablation front ( $\min L_{\nabla T}/L_{\text{tot}}$ ), isentropic Mach number at the ablation front ( $M_s|_{\xi_{\text{af}}}$ ) and maximum value of the isothermal Mach number ( $M_T$ ) and ablation Froude number ( $Fr$ ) (Clarisse *et al.* 2016).

---

$N_{\text{dom}}$	$N_{\text{cheb}}$	$\Delta t_c$
189	50	$1.3 \cdot 10^{-7}$

---

TABLE 2. Numerical characteristic parameters for the base-flow defined in table 1: number of subdomains  $N_{\text{dom}}$ , number of points  $N_{\text{cheb}}$  per subdomain, and critical time-step  $\Delta t_c$  at  $t = 1$ .

---

length of the conduction region evolves as  $l_{\text{cond}} = t^\alpha L_{\text{cond}}$  (see Boudesocque-Dubois *et al.*, 2008, § 4.1).

The range of characteristic lengths of the ablation wave is illustrated by the ratio between the characteristic length of the ablation layer (the local gradient length  $L_{\nabla T} = \bar{G}\bar{\Theta}/d_\xi\bar{\Theta}$ ) and the length of the conduction region in table 1. Such a steep flow requires a suitable numerical method to furnish accurate solutions suitable for a stability analysis. Solutions to (2.8), (2.11) are discretized spatially by a Chebychev pseudospectral scheme on a multidomain grid made of  $N_{\text{dom}}$  subdomains of  $N_{\text{cheb}}$  collocation points each. The solution is computed thanks to a self-adaptive iterative procedure (Gauthier *et al.* 2005; Boudesocque-Dubois *et al.* 2013). For given  $N_{\text{dom}}$  and  $N_{\text{cheb}}$  (table 2), this method computes simultaneously the optimal multidomain grid — i.e. minimizing the approximation error — and the solution to (2.8), (2.11).

### 2.3. Linear perturbations

Any Eulerian dependent variable is perturbed to the first order as

$$f = f^{(0)}(x, t) + \epsilon \tilde{f}(x, y, z, t) + \mathcal{O}(\epsilon^2), \quad \text{with } \epsilon \ll 1.$$

for  $f = \rho, \mathbf{v}, T$ , where  $f^{(0)}$  is a solution to (2.3)-(2.6). Evolution equations for linear perturbations  $\tilde{f}$  are obtained in the coordinate systems  $(x, y, z, t)$ ,  $(m, y, z, t)$  and finally  $(\xi, y, z, t)$  (Clarisse *et al.* 2008).

Although the base flow is self-similar and in slab symmetry, linear perturbations are considered without self-similar assumption. The velocity perturbation field contains a transverse component  $\tilde{\mathbf{v}}_\perp$  in the  $(Oyz)$  plan. With the help of a Helmholtz decomposition of  $\tilde{\mathbf{v}}_\perp$ , the momentum conservation in the transverse direction is replaced by an evolution equation for  $\tilde{d}_\perp = (\partial_y \partial_z) \cdot \tilde{\mathbf{v}}_\perp$ . As the base flow does not depend on the variables  $(y, z)$ , perturbation variables are Fourier-transformed in the  $(Oyz)$  plane, with the transverse wavenumber  $k_\perp = \sqrt{k_y^2 + k_z^2}$ . The Fourier coefficients of the linear perturbations depend on the variables  $(\xi, t)$  and are denoted  $\hat{G}$ ,  $\hat{V}_x$ ,  $\hat{D}_\perp$  and  $\hat{\Theta}$ , for the density, longitudinal

velocity, transverse divergence of the transverse velocity and temperature, respectively. The resulting evolution equations for Fourier coefficients read (Varillon 2019)

$$\partial_t \widehat{\mathbf{U}} + \mathbf{A} \partial_\xi^2 \widehat{\mathbf{U}} + \mathbf{B} \partial_\xi \widehat{\mathbf{U}} + \mathbf{C} \widehat{\mathbf{U}} = \mathbf{0} \quad \Leftrightarrow \quad \partial_t \widehat{\mathbf{U}} = \mathbf{L}(\xi, t) \widehat{\mathbf{U}}, \quad (2.12a)$$

for

$$\widehat{\mathbf{U}} = \begin{pmatrix} \widehat{G} & \widehat{V}_x & \widehat{D}_\perp & \widehat{\Theta} \end{pmatrix}^\top \quad (2.12b)$$

with

$$\mathbf{A} = \begin{pmatrix} 0 & 0 & 0 & 0 \\ 0 & 0 & 0 & 0 \\ 0 & 0 & 0 & 0 \\ 0 & 0 & 0 & t^{-1} C_v^{-1} \bar{G} \bar{\Psi}_{\Theta'} \end{pmatrix}, \quad (2.12c)$$

$$\mathbf{B} = \begin{pmatrix} -\alpha \xi / t & t^{-\alpha} \bar{G}^2 & 0 & 0 \\ t^{\alpha-2} \bar{\Theta} & -\alpha \xi / t & 0 & t^{-\alpha} \bar{G} \\ 0 & 0 & -\alpha \xi / t & 0 \\ t^{2\alpha-3} C_v^{-1} \bar{\Psi}_G & t^{\alpha-2} C_v^{-1} \bar{P} & 0 & B_{44} \end{pmatrix}, \quad (2.12d)$$

$$B_{44} = t^{-1} \left( -\alpha \xi + C_v^{-1} [\mathrm{d}_\xi(\bar{G} \bar{\Psi}_{\Theta'}) + \bar{\Psi}_\Theta] \right)$$

$$\mathbf{C} = \begin{pmatrix} t^{-1} \bar{G} \mathrm{d}_\xi \bar{V}_x & t^{-\alpha} \bar{G} \mathrm{d}_\xi \bar{G} & \bar{G} & 0 \\ -t^{\alpha-2} \bar{\Theta} \mathrm{d}_\xi \bar{G} / \bar{G} & \bar{G} \mathrm{d}_\xi \bar{V}_x / t & 0 & t^{-\alpha} \mathrm{d}_\xi \bar{G} \\ -t^{2(\alpha-1)} k_\perp^2 \bar{\Theta} / \bar{G} & 0 & 0 & -k_\perp^2 \\ C_{41} & t^{\alpha-2} \bar{G} \mathrm{d}_\xi \bar{\Theta} & t^{2(\alpha-1)} C_v^{-1} \bar{\Theta} & C_{44} \end{pmatrix}, \quad (2.12e)$$

$$C_{41} = t^{2\alpha-3} C_v^{-1} (\mathrm{d}_\xi \bar{\Psi}_G - \bar{G}^{-1} \mathrm{d}_\xi \bar{\Psi}),$$

$$C_{44} = t^{-1} C_v^{-1} [\bar{G} \mathrm{d}_\xi \bar{V}_x + \mathrm{d}_\xi \bar{\Psi}_\Theta] - k_\perp^2 t^{2\alpha-1} \bar{G}^{-1} \bar{\Psi}_{\Theta'}.$$

where  $\bar{\Psi}_G$ ,  $\bar{\Psi}_\Theta$  and  $\bar{\Psi}_{\Theta'}$  stand for the partial derivatives of  $\Psi$  (2.10) with respect to  $G$ ,  $\Theta$  and  $\Theta'$ , respectively. The external surface and shock front are also perturbed and their linear deformation Fourier components are denoted  $\widehat{X}_{\text{es}}(t)$  and  $\widehat{X}_{\text{sf}}(t)$ . At the external surface, perturbation in pressure  $\widehat{p}_{\text{es}}(t)$  and heat flux  $\widehat{\varphi}_{\text{es}}(t)$  are imposed. Perturbed boundary conditions arise from a first order expansion of Eq. (2.5) between the mean position of the boundary surface and its perturbed position (Clarisse *et al.* 2008)

$$\widehat{p}_{\text{es}}(t) = \widehat{p}(0, t) + \widehat{X}_{\text{es}}(t) \bar{\rho}(0, t) \partial_m \bar{p}|_{m=0}, \quad (2.13a)$$

$$\widehat{\varphi}_{\text{es}}(t) = \widehat{\varphi}(0, t) + \widehat{X}_{\text{es}}(t) \bar{\rho}(0, t) \partial_m \bar{\varphi}|_{m=0}. \quad (2.13b)$$

As the external surface is a material interface, the following kinematic relation applies

$$\widehat{v}_{\text{es}}(t) = \dot{\widehat{X}}_{\text{es}}(t) = \bar{v}(0, t) + \widehat{X}_{\text{es}}(t) \bar{\rho}(0, t) \partial_m \bar{v}|_{m=0}. \quad (2.13c)$$

At the shock front, Rankine–Hugoniot relations are perturbed and relate the perturbation state upstream of the shock front to shock front deformation and flow perturbations downstream of the shock front (App. A). In both cases, boundary relations take the generic form of the system

$$\mathbf{N}^a \partial_\xi \widehat{\mathbf{U}}|_a + \mathbf{M}^a \widehat{\mathbf{U}}|_a + \widehat{X}_a \mathbf{S}^{a,0} + \dot{\widehat{X}}_a \mathbf{S}^{a,1} = \widehat{\mathbf{F}}^a, \quad \text{for } a = \text{es or sf} \quad (2.14)$$

where the matrices  $\mathbf{N}^a$ ,  $\mathbf{M}^a$  and vectors  $\mathbf{S}^{a,0}$ ,  $\mathbf{S}^{a,1}$  and  $\widehat{\mathbf{F}}^a$  are given in App. A.

Solutions to (2.12), (2.14) are computed on the same grid as for the base flow and integrated in time with a three-step implicit-explicit Runge-Kutta scheme. The stiffness of the ablation front automatically constrains the critical time step  $\Delta t_c$  (table 2). The code computing the base flow and perturbations has been extensively verified against analytical solutions in (Boudesocque-Dubois *et al.* 2003, 2006, 2008; Clarisse *et al.* 2008).

### 3. Optimization problem

We are interested in the solutions to the following optimal initial perturbation (OIP) problem:

*Find the initial state  $(\widehat{\mathbf{U}}, \widehat{\mathbf{X}}_{\text{es}}, \widehat{\mathbf{X}}_{\text{sf}})|_{t_0}$  that maximizes an objective functional  $\mathcal{J}(t_f)$ , with  $(\widehat{\mathbf{U}}, \widehat{\mathbf{X}}_{\text{es}}, \widehat{\mathbf{X}}_{\text{sf}})$  solution to (2.12), (2.14) for zero external forcing.*

As an objective functional, we choose to use the energy of Chu (1965), leading in the present case to the definition

$$\mathcal{J} = \frac{1}{2} \int_{x_{\text{es}}}^{x_{\text{sf}}} \left( \frac{\bar{T}}{\bar{\rho}} \widehat{\rho}^2 + \bar{\rho} (\widehat{v}_x^2 + \widehat{v}_\perp^2) + C_v \frac{\bar{\rho}}{\bar{T}} \widehat{T}^2 \right) dx. \quad (3.1)$$

Chu's energy accounts for acoustic, entropy and kinetic energies. This quantity is conserved for a uniform base flow without internal or boundary source of perturbations. The choice of Chu's energy is motivated by its wide use in thermoacoustic problems and comprise the whole extent of the flow, although it does not account for the energy variation related to boundary deformations. Other energies, such as the energy of Myers (1991), may not be (semi) positive-definite, and thus may not fulfill the condition of being a (semi) norm for perturbations, as it is required for optimization. Chu's energy is a norm for  $\widehat{\mathbf{U}}$  but a semi-norm for  $(\widehat{\mathbf{U}}, \widehat{\mathbf{X}}_{\text{es}}, \widehat{\mathbf{X}}_{\text{sf}})$ . Following (Foures *et al.* 2012), we need to supplement  $\mathcal{J}$  by a complementary semi-norm  $\mathcal{J}^*$  for normalization purpose, such that the direct sum of the kernels of  $\mathcal{J}$  and  $\mathcal{J}^*$  spans the space of solutions. We choose  $\mathcal{J}^* = (\widehat{\mathbf{X}}_{\text{es}}^2 + \widehat{\mathbf{X}}_{\text{sf}}^2)/2$ .

Since ablation flows are nonuniform it is therefore necessary to use a global method. In our case the base flow is time dependent, which leads to a time dependent evolution operator  $\mathbf{L}$  for perturbations. In such a situation, direct-adjoint methods are commonly used: the set of equations (2.12), (2.14), along with initial conditions, constitutes the *direct* problem and its *adjoint* problem is derived. Solving both the direct and adjoint problems simultaneously yields the optimal perturbation. Adjoint problems have been widely used in the field of hydrodynamic stability analysis (see Luchini & Bottaro, 2014 and references therein). Here we chose to derive the adjoint problem from the Lagrange multiplier technique taken from optimal control theory (Gunzburger 1997), but other methods exist to do so, e.g. *via* the derivation of a dual problem (Giles & Pierce 1997, 2000; Luchini & Bottaro 1998) or the projection on a set of test functions (Schmid & Henningson 2001). The Lagrange multiplier technique presents the advantage of furnishing optimality conditions and a gradient direction suitable for the gradient descent algorithm (Guégan *et al.* 2006).

However the majority of stability analyses using adjoint equations deal with incompressible fluids and applications of this method to compressible flows are still rather scarce. The issue of adjoint boundary conditions for hyperbolic systems of equations was treated by Giles & Pierce (1997) within the dual problem approach. Moreover, the dominant practice is by far to exclude boundary conditions — unless they are part of the control variables — from the Lagrange multiplier formulation. The optimization

is then performed in a solution space that is constrained by the desired boundary conditions and the proper adjoint boundary conditions are deduced from considering boundary contributions. The fact that, in our case, boundary conditions are applied on moving boundaries that are subject to their own dynamics and must be found as part of the solution to the problem, brings in an additional complication. An adjoint-based optimization of a steady and incompressible flow with free boundaries is treated in (Volkov *et al.* 2009) with a Lagrange multiplier formulation. But having to deal presently with both a compressible flow and unsteady free boundaries has required us to identify a suitable formulation of the Lagrange functional with limited insights from previous works.

In the present work we derive a continuous adjoint problem (*differentiate then discretize*, cf. Gunzburger, 1997) and not a discrete adjoint obtained from the discretized direct problem (*discretize then differentiate*). This way of proceeding yields a better understanding of the inclusion of the constraints in the Lagrange functional. In addition, the intrication of the different numerical methods we have recourse to in order to integrate in time the direct problem, very classical when considered individually, leads to a level of complexity not well suited for the discrete adjoint approach. In particular, the discrete version of the time evolution operator of perturbations  $\mathbf{L}$  (2.12) is never built, and as a consequence the discrete adjoint does not simply amount to the transconjugate of the discrete version of  $\mathbf{L}$ . Boundary conditions also bring an increased complexity.

### 3.1. Lagrange functional

The Lagrange functional is built by adding the constraints that the state variable must verify to the objective functional with the help of Lagrange multipliers, or adjoint variables (Gunzburger 1997). This formulation obeys the following principle: the constraints enforced for boundary conditions have to be such that the direct problem inferred from the Lagrange functional is well-posed. What is clear for a scalar advection equation requires, in the case of a hyperbolic system, to include constraints only on the incoming characteristics and leave the outgoing characteristics free from constraints. As a consequence, there are as many Lagrange multipliers as there are incoming waves at each boundary. In the present case, system (2.12) rewrites as

$$\begin{aligned} \partial_t \begin{pmatrix} \widehat{U}_I \\ \widehat{U}_{II} \end{pmatrix} + \begin{pmatrix} \mathbf{0} & \mathbf{0} \\ \mathbf{0} & \mathbf{A}_{22} \end{pmatrix} \partial_\xi^2 \begin{pmatrix} \widehat{U}_I \\ \widehat{U}_{II} \end{pmatrix} + \begin{pmatrix} \mathbf{B}_{11} & \mathbf{B}_{12} \\ \mathbf{B}_{21} & \mathbf{B}_{22} \end{pmatrix} \partial_\xi \begin{pmatrix} \widehat{U}_I \\ \widehat{U}_{II} \end{pmatrix} \\ + \begin{pmatrix} \mathbf{C}_{11} & \mathbf{C}_{12} \\ \mathbf{C}_{21} & \mathbf{C}_{22} \end{pmatrix} \begin{pmatrix} \widehat{U}_I \\ \widehat{U}_{II} \end{pmatrix} = \mathbf{0}, \end{aligned} \quad (3.2a)$$

where  $\widehat{\mathbf{U}}_I = (\widehat{G} \ \widehat{V}_x \ \widehat{D}_\perp)^\top$  and  $\widehat{\mathbf{U}}_{II} = \widehat{\Theta}$ . The submatrices  $\mathbf{A}_{xy}$ ,  $\mathbf{B}_{xy}$  and  $\mathbf{C}_{xy}$  with  $x,y=1,2$  are conformal to the subvectors  $\widehat{U}_I$ ,  $\widehat{U}_{II}$ . This system is composed of a parabolic scalar subequation since  $\mathbf{A}_{22} = A_{44}$ , with  $A_{44} < 0$  as a consequence of (2.10), namely

$$\partial_t \widehat{U}_{II} + \mathbf{A}_{22} \partial_\xi^2 \widehat{U}_{II} = 0, \quad (3.2b)$$

and a hyperbolic subsystem for which a Kreiss symmetrizer exists (Kreiss 1970), of size  $3 \times 3$

$$\partial_t \widehat{U}_I + \mathbf{B}_{11} \partial_\xi \widehat{U}_I = \mathbf{0}, \quad (3.2c)$$

corresponding to isothermal gas dynamics. Therefore system (2.12) constitutes an incompletely parabolic system (Strikwerda 1977). The IBVP (2.12), (2.14) is well-posed if, at

Lagrange multipliers	Corresponding constraints	Type
$\widehat{\mathcal{U}}^\dagger(\xi, t)$	Evolution equation for perturbations	4-vector
$\widehat{\mathcal{V}}_{\text{es}}^\dagger(t)$ and $\widehat{\mathcal{V}}_{\text{sf}}^\dagger(t)$	Hyperbolic subsystem BCs	3-vectors
$\widehat{\eta}_{\text{es}}^\dagger(t)$ and $\widehat{\eta}_{\text{sf}}^\dagger(t)$	Parabolic subequation BCs	scalars
$\widehat{\mu}_{\text{es}}^\dagger(t)$ and $\widehat{\mu}_{\text{sf}}^\dagger(t)$	Evolution equation for boundary deformations	scalars

TABLE 3. Lagrange multipliers used in the Lagrange functional (3.3).

each boundary, one condition is applied on the parabolic equation, and one condition is applied on each incoming wave of the hyperbolic subsystem.

Additionally, the deformations  $\widehat{X}_a$  implicitly obey temporal ordinary differential equations (ODEs)

$$d_t \widehat{X}_a = \widehat{X}_a,$$

where the  $\widehat{X}_a$  are determined after the boundary relations (2.14). Therefore, these evolution equations need to be added as constraints in the Lagrange functional. If the above mentioned rules are not verified — e.g. if boundary relations are added in the Lagrange functional as they are expressed in the physical model (2.14) — then the adjoint variables are overdetermined. As a consequence, we form the Lagrange functional

$$\mathcal{L} = \mathcal{J}(t_f) - \mathcal{O} - \sum_{a=\text{es},\text{sf}} (\mathcal{B}_a^h + \mathcal{B}_a^p + \mathcal{F}_a), \quad (3.3)$$

where the different constraints come as follows:

- The term

$$\mathcal{O} = \int_{t_0,0}^{t_f,\xi_{\text{sf}}} \widehat{\mathcal{U}}^{\dagger\top} (\partial_t \widehat{\mathcal{U}} - \mathbf{L}\widehat{\mathcal{U}}) d\xi dt, \quad (3.4)$$

expresses the constraint of satisfying the evolution equation (2.12) for  $\widehat{\mathcal{U}}$ , with the Lagrange multiplier  $\widehat{\mathcal{U}}^\dagger(\xi, t)$  (table 3).

- The term

$$\mathcal{B}_a^h = \int_{t_0}^{t_f} \widehat{\mathcal{V}}_a^{\dagger\top} \mathbf{B}_{11}^{\text{a},\text{in}} (\widehat{\mathcal{U}}|_a - \widehat{\mathcal{U}}_1^{\text{a}}) dt, \quad (3.5)$$

expresses the constraint of satisfying the boundary conditions for the hyperbolic subsystem, with the Lagrange multipliers  $\widehat{\mathcal{V}}_a^\dagger(t)$  (table 3). The matrix  $\mathbf{B}_{11}^{\text{a},\text{in}}$  is the matrix of incoming waves at the boundary ‘a’ (see App. A.3), and therefore the number of components to be determined in  $\widehat{\mathcal{V}}_a^\dagger$  is given by the rank of  $\mathbf{B}_{11}^{\text{a},\text{in}}$ . The set point  $\widehat{\mathcal{U}}_1^{\text{a}}$  is defined in (A 7).

- The term

$$\mathcal{B}_a^p = \int_{t_0}^{t_f} \widehat{\eta}_a^\dagger \widehat{\mathcal{B}}_a^p (\widehat{\mathcal{U}}|_a, \widehat{X}_a) dt, \quad (3.6)$$

expresses the constraint of satisfying the boundary condition on the parabolic subequation, with the scalar Lagrange multipliers  $\widehat{\eta}_a^\dagger$  (table 3). The function  $\widehat{\mathcal{B}}_a^p$  expresses

heat-flux continuity at the external surface and total energy conservation at the shock front and is defined in (A 8).

- The term

$$\mathcal{F}_a = \int_{t_0}^{t_f} \hat{\mu}_a^\dagger \left( d_t \hat{X}_a - \hat{X}_a \right) dt, \quad (3.7)$$

expresses the constraint of satisfying the evolution equation of the boundary deformation, with the Lagrange multipliers  $\hat{\mu}_a^\dagger$  (table 3). The deformation velocity is defined in (A 9). Additionally, we require that the initial condition be normalized,  $\mathcal{J}(t_0) + \mathcal{J}^*(t_0) = \text{cst}$ . Since the system (2.12), (2.14) is linear, it is sufficient to normalize the initial condition to unity,  $\mathcal{J}(t_0) + \mathcal{J}^*(t_0) = 1$ , and to consider different values of the initial distribution

$$r_c = \frac{\mathcal{J}(t_0)}{\mathcal{J}(t_0) + \mathcal{J}^*(t_0)}, \quad (3.8)$$

between 0 and 1.

### 3.2. Adjoint problem

The solution to the OIP problem lies in the stationary points of the Lagrange functional (Gunzburger 1997), i.e. the points for which the variation of  $\mathcal{L}$  with respect to each independent variable  $w$  in any direction  $w'$

$$\nabla_w \mathcal{L} \cdot w' = \lim_{\epsilon \rightarrow 0} \frac{\mathcal{L}(w + \epsilon w') - \mathcal{L}(w)}{\epsilon} \quad (3.9)$$

vanishes. Cancelling the variations of  $\mathcal{L}$  with respect to the direct variable  $\hat{\mathbf{U}}$  yields the *adjoint problem*: evolution equations for the adjoint variables, the Lagrange multipliers in table 3, namely

$$\begin{aligned} \partial_t \hat{\mathbf{U}}^\dagger + \mathbf{A}^\dagger \partial_\xi^2 \hat{\mathbf{U}}^\dagger + \mathbf{B}^\dagger \partial_\xi \hat{\mathbf{U}}^\dagger + \mathbf{C}^\dagger \hat{\mathbf{U}}^\dagger &= \mathbf{0} \quad \Leftrightarrow \quad \partial_t \hat{\mathbf{U}}^\dagger = \mathbf{L}^\dagger \hat{\mathbf{U}}^\dagger, \\ \mathbf{A}^\dagger &= -\mathbf{A}^\top, \quad \mathbf{B}^\dagger = (\mathbf{B} - 2\partial_\xi \mathbf{A})^\top, \quad \mathbf{C}^\dagger = -(\mathbf{C} - \partial_\xi \mathbf{B} + \partial_\xi^2 \mathbf{A})^\top, \end{aligned} \quad (3.10)$$

supplemented by boundary conditions

$$\left( B_{ji} \hat{U}_j^\dagger - \partial_\xi (A_{ji} \hat{U}_j^\dagger) \right) \Big|_{\text{es}} = \Pi_{ij}^{\text{es}} \hat{\nu}_{\text{es}j}^\dagger + M_{4i}^{\text{es}} \hat{\eta}_{\text{es}}^\dagger + \hat{\mu}_{\text{es}}^\dagger M_{2i}^{\text{es}}, \quad (3.11a)$$

$$-A_{44} \hat{U}_4^\dagger \Big|_{\text{es}} + N_{44}^{\text{es}} P_{i4}^{\text{es}} \left( \mathbf{B}_{11}^{\text{in}} \hat{\nu}_{\text{es}}^\dagger \right)_i + \hat{\eta}_{\text{es}}^\dagger N_{44}^{\text{es}} = 0, \quad (3.11b)$$

$$- \left( B_{ji} \hat{U}_j^\dagger - \partial_\xi (A_{ji} \hat{U}_j^\dagger) \right) \Big|_{\text{sf}} = \Pi_{ij}^{\text{sf}} \hat{\nu}_{\text{sf}j}^\dagger + M_{4i}^{\text{sf}} \hat{\eta}_{\text{sf}}^\dagger + \hat{\mu}_{\text{sf}}^\dagger M_{2i}^{\text{sf}}, \quad (3.12a)$$

$$A_{44} \hat{U}_4^\dagger \Big|_{\text{sf}} + N_{44}^{\text{es}} P_{i4}^{\text{sf}} \left( \mathbf{B}_{11}^{\text{in}} \hat{\nu}_{\text{sf}}^\dagger \right)_i + \hat{\eta}_{\text{sf}}^\dagger N_{44}^{\text{sf}} = 0, \quad (3.12b)$$

with  $\mathbf{P}^a = \mathbf{M}_a^{-1}$ ,  $\Pi_{ij} = (\mathbf{B}_{11}^{\text{in}})_{ij}$  for  $i, j = 1, 2, 3$  and  $\Pi_{4j} = 0$  for  $j = 1, 2, 3$ . Cancelling the variations of  $\mathcal{L}$  with respect to the direct variables  $\hat{X}_{\text{es}}$  and  $\hat{X}_{\text{sf}}$  yields scalar ODEs

$$d_t \hat{X}_a^\dagger = \hat{X}_a^\dagger \quad \text{for } a = \text{es, sf}, \quad (3.13)$$

where  $\hat{X}_a^\dagger$  and  $\hat{X}_a^\dagger$  are scalar linear combinations of  $\hat{\mu}_a^\dagger$ ,  $\hat{\nu}_a^\dagger$  and  $\hat{\eta}_a^\dagger$  defined in (B 3). Terminal and initial conditions come as

$$\hat{\mathbf{U}}^\dagger|_{t_f} = \nabla_{\hat{\mathbf{U}}} \mathcal{J}(t_f) \quad , \quad \hat{X}_a^\dagger|_{t_f} = \nabla_{\hat{X}_a} \mathcal{J}(t_f), \quad (3.14a)$$

$$\hat{\mathbf{U}}^\dagger|_{t_0} = \mathbf{0} \quad , \quad \hat{X}_a^\dagger|_{t_0} = 0. \quad (3.14b)$$

The adjoint evolution system (3.10) has the same structure as the direct evolution system (2.12), an incompletely parabolic system, although the boundary value adjoint problem (3.10)-(3.12) is well-posed if it is integrated backward in time, i.e. from the terminal condition (3.14a). Moreover,  $\mathbf{B}_{11}^\dagger = (\mathbf{B}_{11})^\top$ , therefore the hyperbolic subsystem of the adjoint evolution equation (3.10) has the same wave speeds as in the direct evolution equation (2.12). The adjoint solution is computed with the same pseudo-spectral method as the direct problem.

Finding the solution to the OIP problem amounts to solving simultaneously (2.12), (2.14), (3.10), (3.11), (3.12), (3.13) and (3.14). However, (2.12) needs to be integrated forward and (3.10) backward in time, which makes a straight resolution impossible in practice. Therefore, we have recourse to direct-adjoint looping (Gunzburger 1997). The direct and adjoint problems are solved successively and (3.14b) provides us with the gradient of the Lagrange functional  $\mathcal{L}$  with respect to the control parameters  $(\widehat{U}, \widehat{X}_{\text{es}}, \widehat{X}_{\text{sf}})|_{t_0}$

$$\nabla_{\widehat{U}|_{t_0}} \mathcal{L} = \widehat{U}^\dagger|_{t_0} \quad \text{and} \quad \nabla_{\widehat{X}_{\text{a}}|_{t_0}} \mathcal{L} = \widehat{X}_{\text{a}}^\dagger|_{t_0}. \quad (3.15)$$

At the end of the  $q$ -th direct-adjoint loop, this gradient is used to determine a new initial condition  $\widehat{U}^{\dagger q+1}|_{t_0}$  thanks to a gradient descent method. Here we have used power iterations, i.e.  $\widehat{U}^{\dagger q+1}|_{t_0} = \widehat{U}^{\dagger q}|_{t_0}$ , with a renormalization of  $\widehat{U}^{\dagger q+1}|_{t_0}$ . However, the true gradient method (Douglas *et al.* 2000; Foures *et al.* 2013) led to the same results (see App. D).

## 4. Optimal initial perturbations

### 4.1. Choice of parameters

The initial time is arbitrarily set to  $t_0 = 1$ . Because of the self-similarity, a shift of the initial time would not change results if the terminal time and transverse wavenumber are modified appropriately. The terminal time  $t_f$  is varied in an interval whose upper bound represents the end of the shock transit phase for an actual ICF target design (App. C). Hydrodynamic instability studies of ICF implosions usually consider perturbations in spherical harmonics of Legendre mode numbers  $\ell$  in the range  $10 \leq \ell \leq 10^3$  (Haan *et al.* 2015), here equivalently  $0.33 \leq k_\perp \leq 33$ , knowing that curvature effects cannot be omitted for  $\ell \leq 60$  ( $k_\perp \leq 2$ ). The case  $k_\perp = 0$  is also treated, corresponding to longitudinal shifts of the flow.

The optimization process must start from a non-zero first guess. This first guess is taken as the perturbation state obtained at  $t_0$  that results from the evolution of the flow perturbations initiated at some earlier time  $0 < t_* \leq t_0$  with the initial condition (Clarisse *et al.* 2016)

$$\widehat{U}(\xi, t_*) = \widehat{X}_0 \begin{pmatrix} -t_*^{-\alpha} \bar{G} d_\xi \bar{G} \\ -t_*^{-1} \bar{G} d_\xi \bar{V}_x \\ t_*^{\alpha-1} k_\perp^2 \bar{V}_x|_{\text{sf}} (\xi/\xi_{\text{sf}})^{1-1/\alpha} \\ -t_*^{\alpha-2} \bar{G} d_\xi \bar{\Theta} \end{pmatrix}, \quad \widehat{X}_{\text{es}}(t_*) = \widehat{X}_{\text{sf}}(t_*) = \widehat{X}_0. \quad (4.1)$$

where  $\widehat{X}_0$  is the initial deformation of the external surface and shock front. Such an initial condition is an approximation of the perturbation field that would follow from the self-similar ablation of an ablator with an initial defect of its external surface of wavenumber  $k_\perp$  and amplitude  $\widehat{X}_0$ , for times  $t_*$  sufficiently small for the total thickness of the disturbed flow,  $l_{\text{tot}}(t_*)$ , to be much smaller than the perturbation wavelength  $\lambda_\perp$ , i.e.  $k_\perp l_{\text{tot}}(t_*) \ll 1$ . The configuration thus depicted, under this condition of a thin-sheet flow,

---

$t_0$	$t_f$	$D_t = t_f - t_0$	$k_\perp$	$k_\perp L_{\text{cond}}$	$r_c$	$(\widehat{\varphi}_{\text{es}}, \widehat{p}_{\text{es}}, \widehat{U}_u)$
1	[1.01, 3.5]	[0.01, 2.5]	[0, 32]	[0.53, 52]	[0.01, 1]	(0, 0, $\mathbf{0}$ )

---

TABLE 4. Ranges of parameters explored: initial time  $t_0$ , terminal time  $t_f$ , time duration  $D_t$ , transverse wavenumber  $k_\perp$ , the product  $k_\perp L_{\text{cond}}$  relative to the stability criterion (1.1), initial distribution  $r_c$ , external forcing  $(\widehat{\varphi}_{\text{es}}, \widehat{p}_{\text{es}}, \widehat{U}_u)$ .

---

is that of the ablative Richtmyer–Meshkov instability (Goncharov 1999). Consequently, the chosen first guess and the ensuing flow correspond to that of the ARM instability.

The potential existence of several maxima of the objective functional is tested by using three different first guesses: (i) the ARM instability flow introduced above, (ii) a perturbation field resulting from an external heat flux perturbation at  $t < t_0$ , and (iii) an arbitrary uniform perturbation field. These three different first guesses converge to the same OIP. This test does not rule out the possibility that several local maxima exist, but means that using of one or the other initial guess leads to the same maximum.

In the present study we are focusing on the energy gain,

$$\mathcal{G}(t_f) = \frac{\mathcal{J}(t_f)}{\mathcal{J}(t_0)}. \quad (4.2)$$

In that purpose  $\mathcal{J}(t_0)$  cannot vanish, implying that  $r_c$  has to remain strictly positive. The upper bound ( $r_c = 1$ ) corresponds to zero initial deformations ( $\widehat{X}_{\text{es}} = \widehat{X}_{\text{sf}} = 0$ ).

Measurements of Chu’s energy are not accessible by experimental means. Although this quantity provides us with a comprehensive measure of flow perturbations, it is necessary to consider some outputs that reproduce experimentally measurable quantities. A common experimental diagnostic used to detect hydrodynamic perturbations in imploding shells is the *optical depth*, measured by x-ray radiography and defined as the integral of the opacity along photon optical path (Raman *et al.* 2014). In the case of radiation heat conduction (2.1), the opacity writes  $\varkappa = 4 \bar{\rho}^\mu \bar{T}^{3-\nu}$  (Mihalas & Mihalas 1984). Since the medium upstream to the leading shock front is undisturbed, the optical-depth linear perturbation in the longitudinal direction writes

$$\widehat{OD} = \int_{x_{\text{es}}}^{x_{\text{sf}}} (\widehat{\rho} \varkappa_\rho + \widehat{T} \varkappa_T) dx = \int_0^{m_{\text{sf}}} (\widehat{\rho} \varkappa_\rho + \widehat{T} \varkappa_T) \frac{dm}{\bar{\rho}} + \widehat{X}_{\text{es}} \varkappa|_{\text{es}} + \widehat{X}_{\text{sf}} \varkappa|_{\text{sf}}, \quad (4.3)$$

where  $\varkappa_\rho$  and  $\varkappa_T$  stand for the partial derivatives of  $\varkappa$  with respect to the density and the temperature.

#### 4.2. Energy gains

The ablation flow is prone to amplifying small disturbances for a wide range of transverse wavelengths and terminal times, whatever the initial distribution (figures 4a, c). The amplification shows a trend of being larger for large terminal times and for small transverse wavelegnth (figure 4a). Although they are considered as innocuous by the ARM theory, perturbations of large  $k_\perp l_{\text{cond}}$  are subject to a strong amplification (figure 4b). This high amplification of a global norm of perturbations — Chu’s energy — contrasts with amplification results of the sole ablation front deformation known from the ARM instability.

Curves of the gain (figure 4) are not monotonic but display a series of humps and troughs which reflect the multiplicity of phenomena at stake. These phenomena are ana-

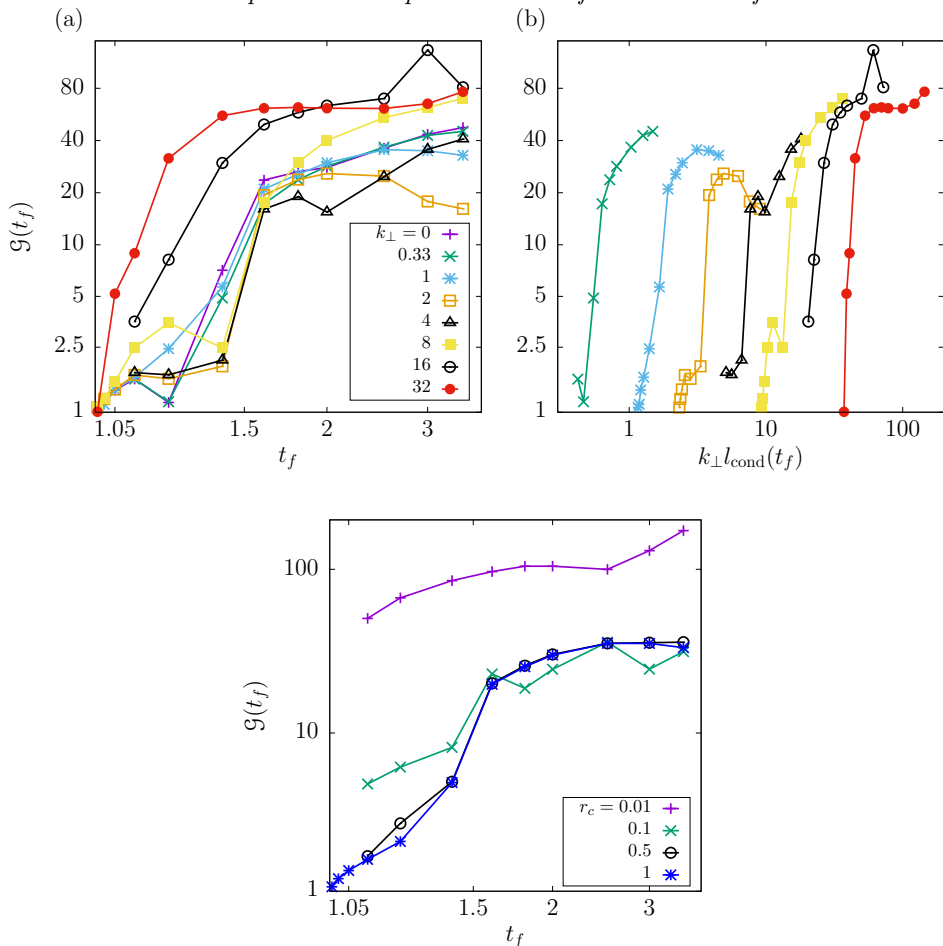


FIGURE 4. Curves of the gain (4.2) for (a) different values of  $k_\perp$  at  $r_c = 1$  with respect to  $t_f$ , (b) same parameters but with respect to  $k_\perp l_{\text{cond}}(t_f)$ , and (c) for different values of  $r_c$  at  $k_\perp = 1$ . The initial time is  $t_0 = 1$ .

lyzed by projecting optimal responses on pseudo-characteristic linear waves proposed in (Varillon *et al.* 2020) as a valuable tool to analyse perturbation evolution in ablation flows. These pseudo-characteristic linear waves are recalled in table 5 and are supplemented by the potential (transverse) vorticity  $\hat{\omega}_\perp / \bar{\rho}$  (Kovácsznay 1953), where

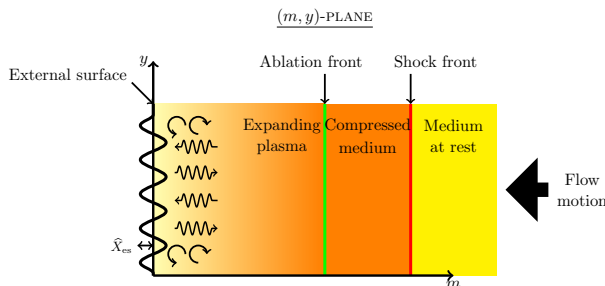
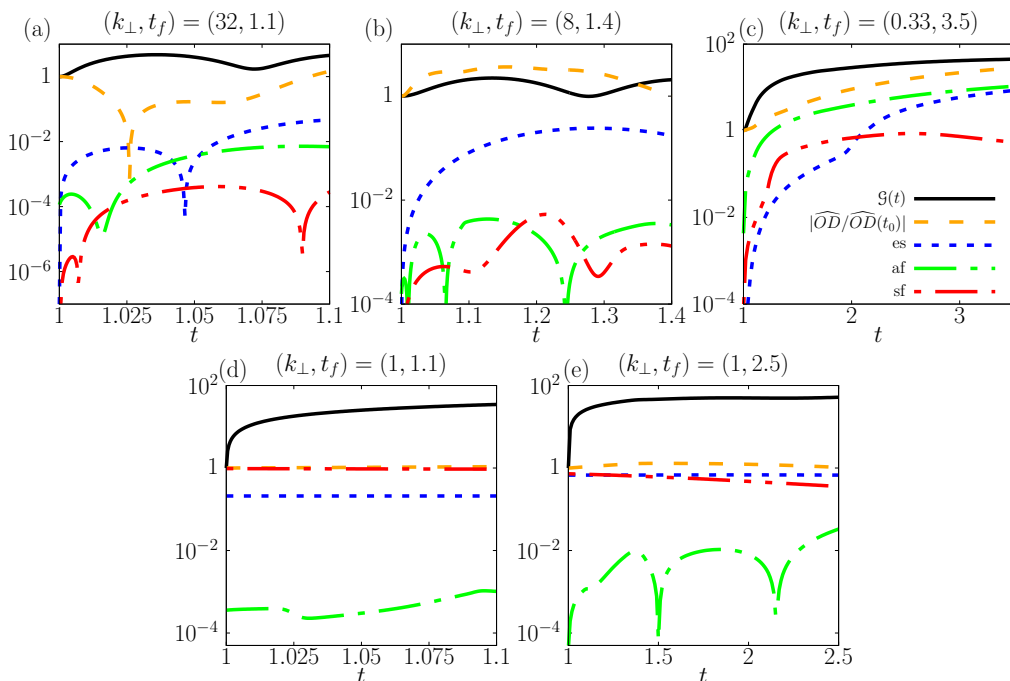
$$\hat{\omega}_\perp = \frac{\bar{\rho}}{i k_\perp} \partial_m \hat{d}_\perp - i k_\perp \hat{v}_x, \quad \text{for } k_\perp > 0. \quad (4.4)$$

The ranges of parameter explored are summarized in table 4.

#### 4.2.1. Short-time growth

For small terminal times ( $t_f = 1.1$ ), OIPs develop in time as a spatially structured signal localized close to the external surface (figure 7), corresponding to acoustic–vorticity interaction (figure 5). Since the time duration  $D_t = t_f - t_0$  is shorter than the travel time of acoustic waves between interfaces, the ablation layer and the shock front play no role in the optimal growth mechanism and their deformations remain negligible (figure 6a). Since the optimal response develops in the vicinity of the external surface, this sole interface is coupled to the perturbation field (figure 6a). The optimal growth mechanism

	Conduction region	Post-shock region
$\mathcal{C}_1$	Heat conductivity	Forward quasi-isentropic acoustic
$\mathcal{C}_2$	Forward quasi-isothermal acoustic	Quasi-entropy
$\mathcal{C}_3$	Transverse velocity	Transverse velocity
$\mathcal{C}_4$	Backward quasi-isothermal acoustic	Backward quasi-isentropic acoustic

TABLE 5. Identification of the pseudo-characteristic waves as proposed in (Varillon *et al.* 2020).FIGURE 5. Schematic view of the optimal growth mechanism: *acoustic-vorticity interaction*, in the  $(m, y)$  plane at a given time  $t > t_0$ . Sinusoidal arrows: acoustics; circular arrows: vorticity.FIGURE 6. Deformation absolute values  $|\widehat{X}|$  of the external surface (es), ablation front (af), and shock front (sf), gain of Chu's energy  $\mathcal{G}(t)$  and normalized absolute values of optical depth perturbation ( $|\widehat{OD}(t)/\widehat{OD}(t_0)|$ ) of the optimal responses. For  $r_c = 1$ : (a)  $(k_\perp, t_f) = (32, 1.1)$ , (b)  $(k_\perp, t_f) = (8, 1.4)$ , (c)  $(k_\perp, t_f) = (0.33, 3.5)$ . For  $r_c = 0.01$ : (d)  $(k_\perp, t_f) = (1, 1.1)$  and (e)  $(k_\perp, t_f) = (1, 2.5)$ .

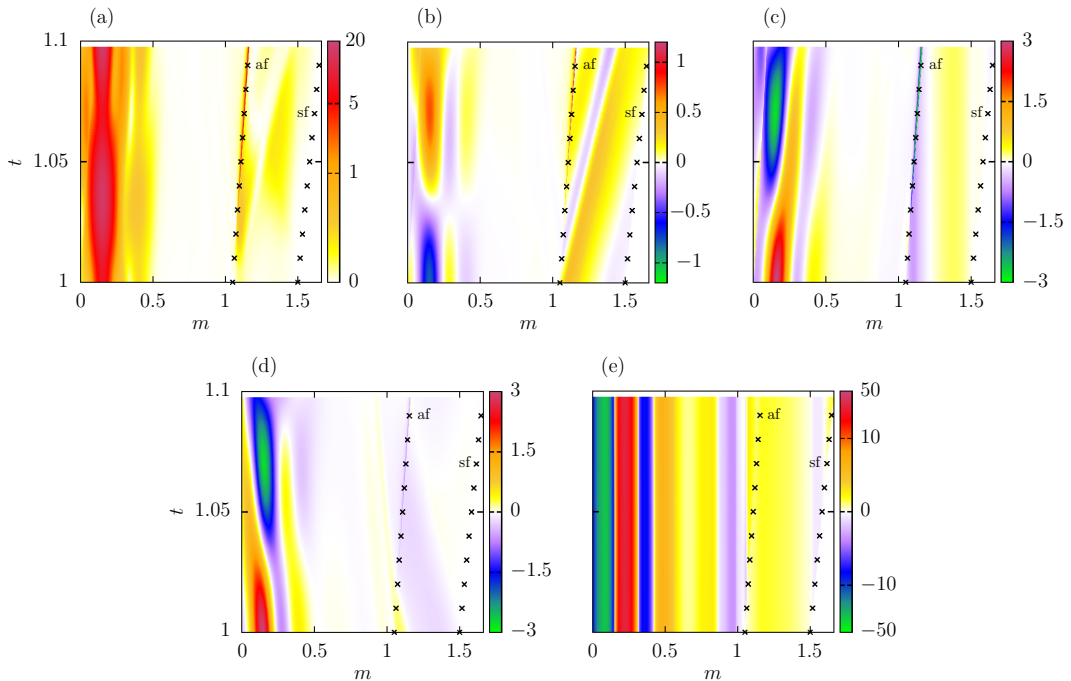


FIGURE 7. Intensity map in the coordinates  $(m, t)$  of the optimal response for  $(k_{\perp}, r_c) = (32, 1)$  and  $t_f = 1.1$ . The external surface is located at  $m = 0$  and trajectories of the ablation front (af) and shock wave (sf) are reported with crosses. The region  $m \geq m_{sf}(t)$  correspond to the unshocked ablator described by (2.6) without perturbations. (a) Chu's energy density. Projection on the pseudo-characteristic variables of table 5 (b)  $\mathcal{C}_1$ , (c)  $\mathcal{C}_2$ , (d)  $\mathcal{C}_4$  plus (e) potential vorticity  $\hat{\omega}_{\perp}/\bar{\rho}$  (4.4).

results from local interactions between spatially structured acoustic and vorticity waves located in the vicinity of the external surface, hereafter referred to as *acoustic–vorticity interactions* (figures 5 and 7b-d). This spatial structure also makes Chu's energy response strongly fluctuating in space and time (figures 6a and 7a).

#### 4.2.2. Long-time growth

As  $t_f$  grows and  $k_{\perp}$  decreases, a transformation of the optimal initial perturbation sets up, from acoustic–vorticity interactions to a signal localized in the ablation layer and compression region with no well-defined structure (figure 8). The dominant mechanisms are long range interactions coupling the ablation layer and shock front (figure 10). Because the time duration  $D_t$  becomes larger than the travel time of acoustic waves between the shock front and the ablation layer ( $t_f = 1.4$ ), an additional growth mechanism arises in the compression region. Forward acoustic waves travel from the ablation layer up to the shock front which re-emits vorticity and entropy waves (figures 8a-d). This is the early stage of the coupling between the ablation layer and the shock front (*af–sf coupling*). Acoustic–vorticity interaction coexists with af–sf coupling at intermediary terminal times, without interacting together (figure 8a), but disappears in front af–sf coupling for large  $t_f$ . For large terminal times corresponding to the end of the shock-transit phase ( $t_f = 3.5$ ), as the time duration equals a few times the travel time of acoustic waves in the compression region, the shock front and ablation layer are strongly coupled and perturbations in the

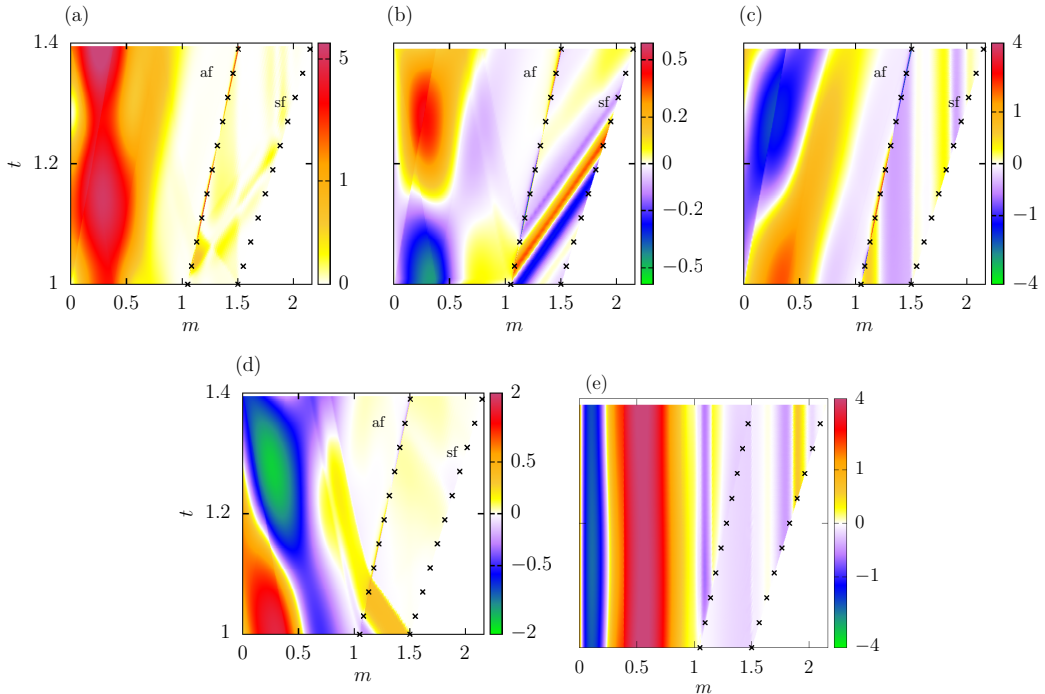


FIGURE 8. Intensity map in the coordinates  $(m, t)$  of the optimal response for  $(k_{\perp}, r_c) = (8, 1)$  and  $t_f = 1.4$ . Labels similar to figure 7. (a) Chu's energy density. Projection on the pseudo-characteristic variables of table 5 (b)  $\mathcal{C}_1$ , (c)  $\mathcal{C}_2$ , (d)  $\mathcal{C}_4$  plus (e) potential vorticity  $\widehat{\omega}_{\perp}/\bar{\rho}$  (4.4).

ablation front dominate those contained in the conduction and compression regions. This makes ablation and shock front deformations much larger (figure 6c).

The resulting optimal growth mechanism evolves from local interactions between acoustic and vorticity waves, without interactions between interfaces, to a regime of coupled shock front and ablation layer (figure 10) where Chu's energy is mostly located in the ablation layer. The ratio of vorticity to acoustic-like content is assessed thanks to the following ratio

$$R = \sqrt{\frac{\int \widehat{\omega}|_{t_0}^2 dx}{\int \widehat{\text{div}} \widehat{\mathbf{v}}|_{t_0}^2 dx}}. \quad (4.5)$$

The acoustic-like content of the OIPs is much greater than the vorticity content (table 6). These ratios support the fact that acoustic waves are the dominant mechanism in the most detrimental perturbations, bearing interactions between ablation and shock front. The expansion velocity of the ablation wave in the conduction region reaches a sufficiently high value so that forward acoustic waves arising from the external surface cannot reach the ablation front within the time interval. Therefore, perturbations arising from the external surface reach the ablation front only by means of heat diffusion, which is less efficient than propagation in transmitting perturbations.

### 4.3. Optimal initial boundary deformations

For an initial perturbation concentrated in the deformations rather than in the flow (case  $r_c = 0.01$ , i.e.  $\mathcal{J}^*(t_0) \gg \mathcal{J}(t_0)$ ), the distribution of the initial deformation is a dominant shock front deformation ( $\widehat{X}_{\text{sf}}|_{t_0}$ ) and a negligible external surface deformation

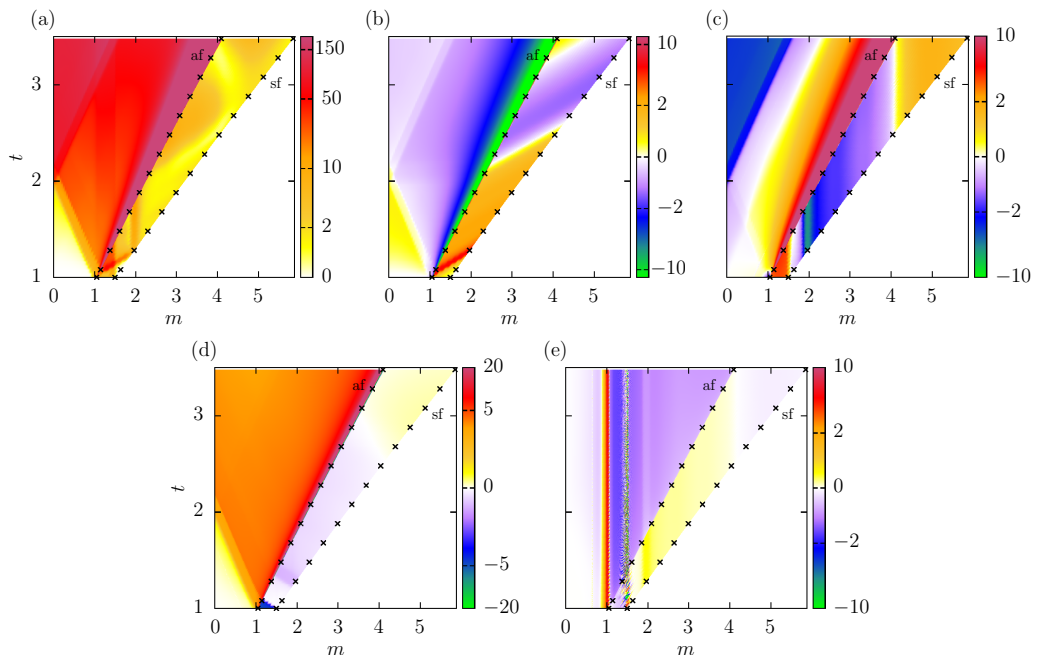


FIGURE 9. Intensity map in the coordinates  $(m, t)$  of the optimal response for  $(k_{\perp}, r_c) = (0.33, 1)$  and  $t_f = 3.5$ . Labels similar to figure 7. (a) Chu's energy density. Projection on the pseudo-characteristic variables of table 5 (b)  $\mathcal{C}_1$ , (c)  $\mathcal{C}_2$ , (d)  $\mathcal{C}_4$  plus (e) potential vorticity  $\widehat{\omega}_{\perp}/\bar{\rho}$  (4.4).

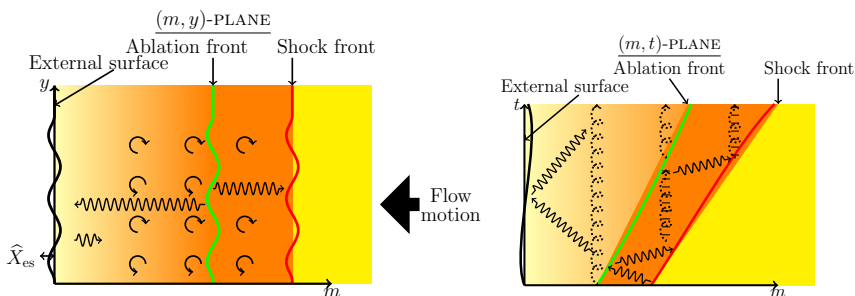


FIGURE 10. Schematic view of the optimal growth mechanism: af-sf coupling, in the  $(m, y)$  plane (left) and in the  $(m, t)$  plane (right). Sinusoidal arrows: acoustics, circular and dashed coil arrows: vorticity, dashes: entropy.

---

$(k_{\perp}, t_f)$	(0.33, 3.5)	(2, 3.5)	(4, 1.8)	(8, 1.4)	(8, 3.5)	(32, 1.1)	(32, 3.5)
OIP	0.17	$5.95 \cdot 10^{-2}$	$1.47 \cdot 10^{-2}$	$2.39 \cdot 10^{-2}$	3.78	0.33	0.69
ARM	0.21	0.29	—	2.00	2.00	31.1	31.1

---

TABLE 6. Ratios of vorticity to acoustic-like content  $R$  (4.5) of some OIPs for  $r_c = 1$  and the corresponding the ARM instability initial perturbation.

---

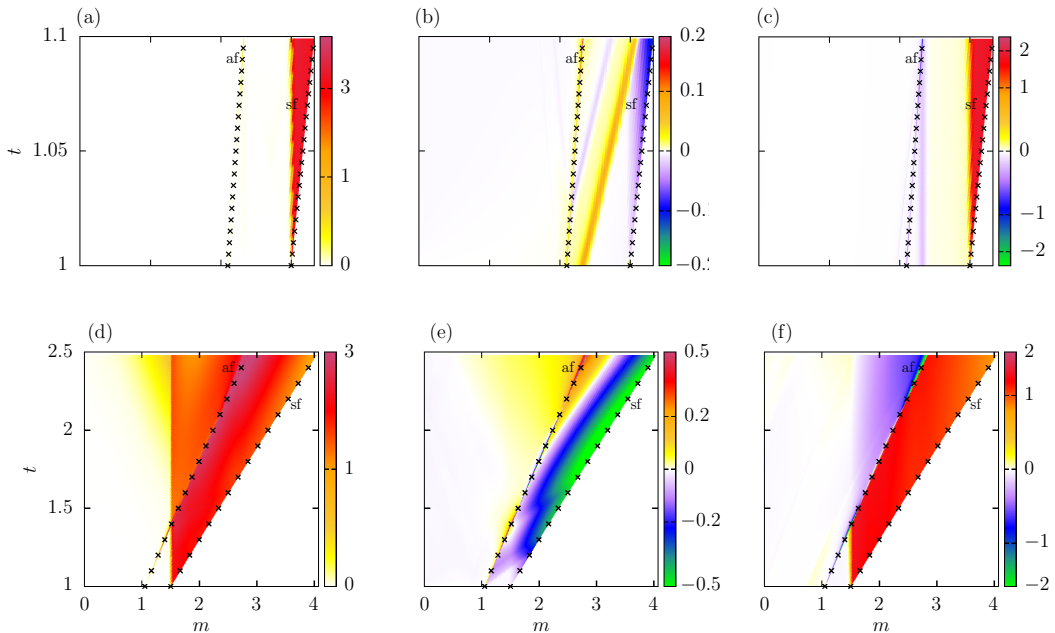


FIGURE 11. Intensity map in the coordinates  $(m, t)$  of the optimal response for  $(k_{\perp}, r_c) = (1, 0.01)$ , with  $t_f = 1.1$  (a)-(c) and  $t_f = 2.5$  (d)-(f). Labels similar to figure 7. Chu's energy density (a) and (d). Projection on the pseudo-characteristic variables of table 5  $\mathcal{C}_1$ : (b) and (e),  $\mathcal{C}_2$ : (c) and (f).

$(\widehat{X}_{\text{es}}|_{t_0})$ , for both long and short terminal times  $t_f$  (figures 6d,e). The OIP in the flow consists in a small forward acoustic signal in the vicinity of the shock front (figure 11). As the shock front deformation is relatively steady (figures 6d,e), it produces an entropy and vorticity signal uniform in space and time. We do not observe any acoustic retroaction of the ablation layer on the shock front, which is therefore subject to its own dynamics (figure 11). The ablation front is stimulated by the entropy and vorticity emitted by the shock front and oscillates. Strictly speaking, there is no af–sf coupling, even for  $t_f = 2.5$  in the case of an initial deformation ( $r_c \ll 1$ ). If the af–sf coupling eventually sets up, it takes a longer time than in the initial distribution case —  $r_c = 1$  — which displays a dominant af–sf coupling for  $t_f \geq 1.8$ . We additionally note that at the shock front, backward acoustics is barely stimulated by incident (acoustic) perturbations which are reflected mostly as entropy and vorticity waves.

#### 4.4. Comparison with the ablative Richtmyer–Meshkov instability

The interest of a systematic search of the OIP *via* a non-modal analysis, beyond the restricted frame of ARM-like initial perturbation, is exemplified on figure 12. The ARM instability initial condition (4.1) reproduces the configuration under which the ARM stability results (1.1) have been obtained. The amplification  $\mathcal{G}(t)$  of (4.1) is compared to optimal gain curves  $\mathcal{G}(t_f)$  in the same configuration:  $r_c = 1$  and  $1.01 \leq t_f \leq 3.5$  (the ARM instability initial condition 4.1 yields  $r_c > 0.99$ ).

For all terminal times and wavelengths tested, the OIP yields a higher amplification than that of the ARM instability initial condition (given that the ARM instability initial condition was used as first guesses). In other words, there is always an initial perturbation that yields an amplification of Chu's energy that is higher than the one induced by the

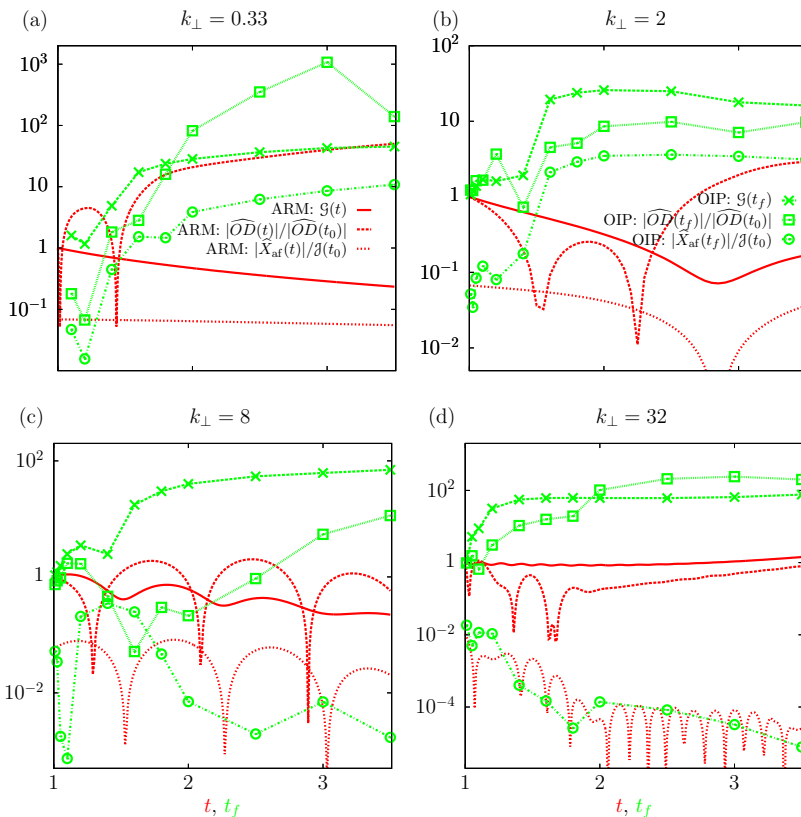


FIGURE 12. Amplification  $\mathcal{G}(t)$  for the ablative Richtmyer–Meshkov instability (ARM) at different  $k_{\perp}$  and optimal gain curve  $\mathcal{G}(t_f)$  in the same configurations. For each case, the optical depth amplification and normalized ablation front deformation are reported, i.e.  $|\widehat{OD}(t)|/|\widehat{OD}(t_0)|$  and  $|\widehat{X}_{af}(t)|/\beta(t_0)$  for the ARM and  $|\widehat{OD}(t_f)|/|\widehat{OD}(t_0)|$  and  $|\widehat{X}_{af}(t_f)|/\beta(t_0)$  for the OIP.

ARM instability initial condition (4.1). Moreover, the flow responses to OIPs shows much more complexity than responses to the ARM instability initial conditions, with numbers of acoustic, entropy and vorticity interactions in the compression region (e.g. compare the response in figure 9 for the OIP at  $(k_{\perp}, t_f) = (0.33, 3.5)$  with that of figure 13 for the ARM instability initial condition).

The responses of the flow in terms of Chu’s energy and in terms of the ablation front deformations are clearly different, which leads to a different appreciation of the flow stability. For OIPs, highest ablation front deformations occur for the largest wavelengths investigated (figures 12a,b). Although this trend complies with the ARM instability results, ablation front deformations resulting from OIPs are higher than the one resulting from the ARM instability initial condition with identical initial value of Chu’s energy. The vorticity content with respect to the acoustic content of the ARM instability initial condition is higher than in the case of the OIPs (table 6). In particular, the vorticity content greatly increases with  $k_{\perp}$  for the ARM instability, which is not observed for the OIPs.

This point emphasises the necessity of a complete non-modal stability analysis, in that such an analysis is not based on the sole least stable mode and does not presume any particular shape of the initial condition.

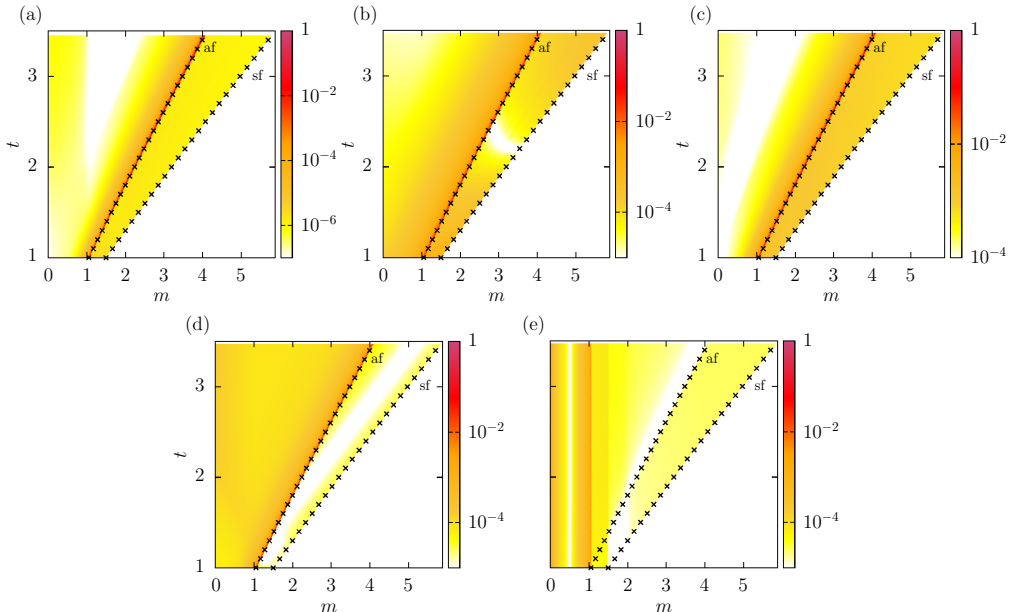


FIGURE 13. Intensity map in the coordinates  $(m, t)$  in logscale of the response to the ARM instability (4.1) with  $t_* = t_0$  for  $k_{\perp} = 0.33$  and  $t_0 \leq t \leq 3.5$ , and that yields responses of figure 12a. (a) Chu's energy density. Projection on the pseudo-characteristic variables of table 5 (b)  $\mathcal{C}_1$ , (c)  $\mathcal{C}_2$ , (d)  $\mathcal{C}_4$  and (e) potential vorticity  $\hat{\omega}_{\perp}/\bar{\rho}$  (4.4).

For small wavelengths (figures 12c,d), ablation front deformations resulting from OIPs agree with the level of that of the ARM instability. However, Chu's energy amplifications are two orders of magnitude higher in the case of OIPs.

## 5. Discussion

The present analysis reveals that the whole ablation flow, and not the sole ablation front, is prone to amplifying perturbations over a wide range of wavelengths at the end of the shock transit phase. This result differs from the one resulting from the ARM instability which was for a long time considered as the dominant destabilizing mechanism. However, such a result is consistent with the recent experimental evidences (Smalyuk *et al.* 2015) of important amplifications of internal ablator perturbations over a wide range of wavelengths during this same phase of an ICF target implosion. We notice a higher sensitivity of the ablation flow to initial perturbations located between the ablation front and the shock front than to the initial perturbations corresponding to the ARM instability. This high sensitivity of the compression region is pictured on figure 14 since, at  $t_0$ , the adjoint variables at the optimum represent the sensitivity of the objective functional to initial perturbations. The sensitivity to longitudinal velocity perturbations is much higher than to density perturbations, in the ablation front and the compression region. The consequences of this sensitivity to longitudinal velocity perturbations are not measurable with current experimental diagnostics, i.e. optical depth or areal mass. The sensitivity is also much higher regarding initial deformations of the shock front ( $r_c \ll 1$ ). These results are intrinsic to the fluid evolution equations, together with the equation of state and non-linear heat-conduction, in this region, and not to a specific ablator or self-similar behaviour. The results differ from previous analyses by the chosen method

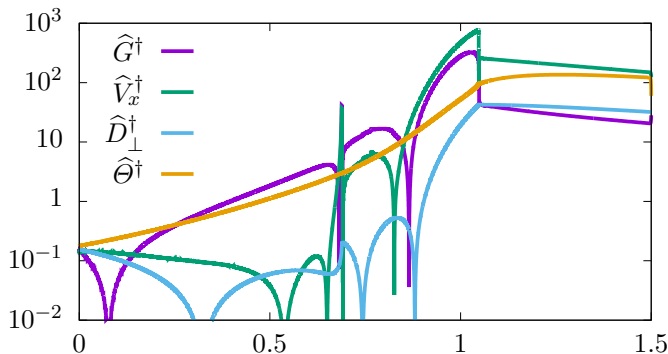


FIGURE 14. Values at  $t_0$  of the adjoint variables at the optimum, or sensitivity of the objective functional to initial perturbations, for  $r_c = 1$ ,  $(k_\perp, t_f) = (2, 3)$ .

of stability analysis — i.e. non-modal analysis — and not because of modelling choices, which are similar to most of the models found in the literature for studying ablation front stability.

In the present study, we have determined some optimal perturbations at an ‘initial’ time  $t_0 > 0$  containing significant vorticity and acoustic perturbations. We may rightly wonder whether such initial conditions are realistic. The fact that the ablation flow has already evolved from its initial state at rest ( $t = 0$ ) up to the time  $t_0$  at which the OIP is defined and that this previous evolution consists of the forerunning shock front travelling through a potentially inhomogeneous medium — the upstream unshocked portion of the ablator — indicates that vorticity and acoustic fields are indeed present in the wake of the shock front since it travelled through a medium with density inhomogeneities (e.g. Huete *et al.* 2012). Therefore ending up with OIPs consisting of acoustic and vorticity fields is fully compatible with a previous evolution of the ablation flow under realistic conditions, the next question that logically comes to mind being then which particular initial states of the unshocked ablator can possibly induce such OIPs?

The present study is based on Chu’s energy, which is a global norm consisting of a kinetic and a potential part, the latter splitting into compression and heat-exchange (Chu 1965). This choice reveals that perturbations in ablation flows are not limited to the sole ablation front deformation. However, semi-norms could be considered, either global in space but only accounting for a specific part of the perturbation energy, or partial in space. As examples, the norm could be defined over the sole post-shock region, or as the square of the ablation front deformation, which is not a perturbation energy but a valuable quantity in the ICF context. This would require defining a window for the integration in space of an energy density, such as in (Lemke *et al.* 2014) for flame fronts. In particular, the use of a measure of the ablation front deformation as an objective functional for an OIP problem implies some mathematical complexity for the definition of the complementary norm that has yet to be overcome. Accounting for external surface and shock front deformations in a global norm *via* a conservation framework similar to (Chu 1965) also remains an open question. In the results presented here, the optical depth perturbation does not allow us to differentiate between low and high Chu’s energy amplifications, owing to the fact, among others, that the velocity field does not affect optical depth.

For these reasons, the questions of, on the one hand, experimental measurements capable to detecting perturbations in a more complete way, and on the other hand,

the choice of an appropriate norm for perturbations, in order to study the stability of ablation flows, appears to be crucial.

## 6. Conclusion

In the present work we have conducted a global non-modal stability analysis to compute the most detrimental initial perturbations in a self-similar ablation wave representative of the shock transit phase of ICF target implosions driven by x rays. The ablation wave is modelled thanks to the compressible Euler equations with nonlinear heat conduction and perturbations are linear and three dimensional. The whole extent of the ablation wave is described, with deformations of the external surface, ablation layer and shock front. Optimal initial perturbations (OIPs) are obtained by direct-adjoint iterations. The adjoint problem is derived using the Lagrange multiplier technique. A proper method is proposed, to build a Lagrange functional correctly accounting for the free boundary deformations and the structure of the evolution equation, which are two inherent characteristics of the problem.

Optimal initial perturbations exhibit the general inclination of ablation flows to amplify perturbations, for a wide range of transverse wavenumbers — i.e. for Legendre modes ranging from 0 to  $10^3$  — and terminal times up to the end of the shock transit phase. Although perturbations of small transverse wavelength compared to the size of the conduction region are considered as innocuous by the theory of the ablative Richtmyer–Meshkov (ARM) instability, they are subject to a strong transient amplification, in particular at the end of the shock transit phase. This result is consistent with the experimental evidences of important amplification of perturbations originating from internal defects of the ablator, for a wide range of wavelengths (Ali *et al.* 2018). The comparison of OIP evolutions with the perturbation developing from the ablative Richtmyer–Meshkov configuration shows an over amplification of OIPs compared to the ARM perturbations. Therefore, most detrimental perturbations must be searched for outside the scope of the ARM configuration.

The analysis shows that perturbations are not only amplified in the ablation layer but in the whole flow. The ablation flow is particularly sensitive to perturbations in the compression region, between the forerunning shock front and the ablation layer. These OIPs in the compression region are consistent with perturbations left by a shock front propagating in an inhomogeneous medium, which points out bulk inhomogeneities of the ablator material as a major source of flow perturbations. The question of the nature and size of the bulk ablator defects capable of inducing the largest perturbation in the ablation wave could be answered *via* a receptivity analysis of the ablation wave to upstream perturbations. Although numerous works have been dedicated to studying the interaction of one — or several — shock waves with a field of perturbations, the above mentioned receptivity problem has never been considered. Finally, to complement the use of Chu’s energy norm, alternative objective functionals based on ablation front deformations would be useful, but induce some mathematical issues with their definition that have yet to be solved. The general idea is to tend to *optimal design* methods applied to ICF target design, such as those that have now been in use for several decades in aerodynamics and thermoacoustics.

The authors are grateful to A. Lefebvre-Lepot and F. Alouges for their discussion and advice concerning the Lagrange functional.

## Appendix A. Boundary conditions for linear perturbations

Here we give the entries of matrices  $\mathbf{N}^a$ ,  $\mathbf{M}^a$  and vectors  $\mathbf{S}^{a,0}$ ,  $\mathbf{S}^{a,1}$  and  $\widehat{\mathbf{F}}^a$  as defined in (2.14).

### A.1. Boundary conditions at the external surface (*es*)

Relations of (2.13) in the coordinate  $(m, t)$  are transformed in the coordinates  $(\xi, t)$ . System (2.13) is supplemented by a trivial equation on  $\widehat{D}_\perp$  so that the matrix  $\mathbf{M}^{\text{es}}$  is invertible. Therefore,

$$\mathbf{M}^{\text{es}} = \left( \begin{array}{cccc} t^{2\alpha-2}\bar{\Theta} & 0 & 0 & \bar{G} \\ 0 & 1 & 0 & 0 \\ 0 & 0 & 1 & 0 \\ t^{3\alpha-3}\Psi_G & 0 & 0 & t^{\alpha-1}\Psi_\Theta \end{array} \right) \Big|_{\text{es}}, \quad \mathbf{S}^{\text{es},0} = \left( \begin{array}{c} t^{-\alpha}\bar{G}d_\xi\bar{P} \\ t^{-1}\bar{G}d_\xi\bar{V} \\ 0 \\ t^{2\alpha-3}\bar{G}d_\xi\bar{\Phi} \end{array} \right) \Big|_{\text{es}},$$

$$\mathbf{S}^{\text{es},1} = \left( \begin{array}{c} 0 \\ -1 \\ 0 \\ 0 \end{array} \right), \quad \text{and} \quad \mathbf{N}^{\text{es}} = \left( \begin{array}{cccc} 0 & 0 & 0 & 0 \\ 0 & 0 & 0 & 0 \\ 0 & 0 & 0 & t^{\alpha-1}\bar{G}\Psi_{\Theta'} \end{array} \right) \Big|_{\text{es}}, \quad (\text{A } 1)$$

$$\widehat{\mathbf{F}}^{\text{es}} = \left( \begin{array}{c} \widehat{P}_{\text{es}}(t) \\ 0 \\ \widehat{D}_\perp|_{\text{es}} \\ \widehat{\Phi}_{\text{es}}(t) \end{array} \right).$$

### A.2. Boundary conditions at the shock front (*sf*)

Boundary conditions for perturbations at the shock front are obtained by the linear perturbation of Rankine–Hugoniot relations in the coordinates  $(x, y, z, t)$  (Clarisse *et al.* 2008, App. B.1). These relations are then transformed in the coordinates  $(m, y, z, t)$  and  $(\xi, y, z, t)$ , and then Fourier transformed in the transverse direction (*Oyz*). Relations between the Fourier coefficients read as in (2.14), where the entries of the matrices and

vectors read,

$$\mathbf{M}^{\text{sf}} = \left( \begin{array}{ccc|cc} t^{\alpha-1}\bar{U}_x & & -\bar{G} & 0 & 0 \\ t^{2\alpha-2}(\bar{U}_x\bar{V}_x - \bar{\Theta}) & & t^{\alpha-1}\bar{G}(\bar{U}_x - \bar{V}_x) & 0 & -\bar{G} \\ 0 & & 0 & 1 & 0 \\ t^{3\alpha-3}M_{41}^{\text{sf}} & & t^{2\alpha-2}(\bar{G}\bar{V}_x(\bar{U}_x - \bar{V}_x/2) - C_P\bar{P}) & 0 & t^{\alpha-1}M_{44}^{\text{sf}} \end{array} \right) \Big|_{\text{sf}}$$

$$M_{41}^{\text{sf}} = C_v(\bar{W} - \gamma\bar{V}_x)\bar{\Theta} + \bar{U}_x\bar{V}_x^2/2 - \bar{\Psi}_G, \quad M_{44}^{\text{sf}} = C_v\bar{G}(\bar{W} - \gamma\bar{V}_x) - \bar{\Psi}_T$$

$$\mathbf{S}^{\text{sf},0} = \left( \begin{array}{c} t^{-1}\bar{G}d_\xi(\bar{G}\bar{U}_x)|_d \\ t^{\alpha-2}\bar{G}d_\xi(\bar{G}\bar{V}_x\bar{U}_x - \bar{P})|_d \\ t^{\alpha-1}k_\perp^2[\bar{V}_x]_d^u \\ t^{2\alpha-3}\bar{G}d_\xi[(C_v\bar{P} + \bar{G}\bar{V}_x^2/2)\bar{U}_x - \bar{P}\bar{V}_x - \bar{\Phi}]|_d \end{array} \right), \quad (\text{A } 2)$$

$$\mathbf{S}^{\text{sf},1} = \left( \begin{array}{c} [\bar{G}]_d^u \\ t^{\alpha-1}[\bar{G}\bar{V}_x]_d^u \\ 0 \\ t^{2\alpha-2}[C_v\bar{P} + \bar{G}\bar{V}_x^2/2]_d^u \end{array} \right), \quad \mathbf{N}^{\text{sf}} = \left( \begin{array}{cccc|c} 0 & 0 & 0 & 0 & 0 \\ 0 & 0 & 0 & 0 & 0 \\ 0 & 0 & 0 & 0 & 0 \\ 0 & 0 & 0 & -t^{\alpha-1}\bar{G}\bar{\Psi}_{\Theta'} & 0 \end{array} \right) \Big|_{\text{sf}},$$

where  $\bar{U}_x = \bar{W} - \bar{V}_x$  is the shock front velocity with respect to the the fluid and  $\bar{W}$  is the shock front velocity in the reference frame. The upperscripts and subscripts  $u$  and  $d$  refer to upstream and downstream from the shock front, respectively.

### A.3. Matrices of the incoming waves at each boundary

As stated in §3.1, system (2.12) is incompletely parabolic: i.e. it is made up of a hyperbolic subsystem composed of the components  $(\hat{G}, \hat{V}_x, \hat{D}_\perp)^\top$  which is supplemented by a parabolic equation involving temperature  $\hat{\Theta}$ . Therefore  $\mathbf{B}_{11}$  (see 3.2) has real valued eigenvalues and defines a system of characteristic waves whose propagation velocities are the eigenvalues. Let  $\mathbf{R}_{11}$  be the matrix of the right eigenvectors and  $\mathbf{D}_{11} = \text{diag}\{\lambda_i, i = 1, 2, 3\}$  with  $\lambda_i$  the eigenvalues, such that

$$\mathbf{B}_{11} = \mathbf{R}_{11}\mathbf{D}_{11}\mathbf{R}_{11}^{-1}.$$

At each side (a = es or sf) we define the matrix of incoming waves

$$\mathbf{B}_{11}^{\text{a,in}} = \mathbf{R}_{11}\mathbf{D}_{11}^{\text{a,in}}\mathbf{R}_{11}^{-1}, \quad (\text{A } 3)$$

and outgoing waves

$$\mathbf{B}_{11}^{\text{a,out}} = \mathbf{R}_{11}\mathbf{D}_{11}^{\text{a,out}}\mathbf{R}_{11}^{-1}, \quad (\text{A } 4)$$

with

$$\mathbf{D}_{11}^{\text{es,in}} = \text{diag}\{\max\{\lambda_i|_{\text{es}}, 0\}\}, \quad \mathbf{D}_{11}^{\text{sf,in}} = \text{diag}\{\min\{\lambda_i|_{\text{sf}}, 0\}\}, \\ \mathbf{D}_{11}^{\text{es,out}} = \text{diag}\{\min\{\lambda_i|_{\text{es}}, 0\}\} \quad \text{and} \quad \mathbf{D}_{11}^{\text{sf,out}} = \text{diag}\{\max\{\lambda_i|_{\text{sf}}, 0\}\},$$

with  $i = 1, 2, 3$ . The matrices  $\mathbf{B}_{11}^{\text{a,in}}$  project the information on the incoming characteristics of the hyperbolic subsystem in the space of primitive variables.

The matrix  $\mathbf{B}$  also proves to be hyperbolic. Therefore we can similarly define  $\mathbf{B}^{\text{a,in}}$  and  $\mathbf{B}^{\text{a,out}}$  as

$$\mathbf{B}^{\text{a,in/out}} = \mathbf{R}\mathbf{D}^{\text{a,in/out}}\mathbf{R}^{-1}, \quad (\text{A } 5)$$

with  $\mathbf{R}$  the matrix of the right eigenvectors of  $\mathbf{B}$ ,  $\mathbf{D} = \text{diag}\{\beta_i, i = 1, \dots, 4\}$ ,  $\beta_i$  the eigenvalues of  $\mathbf{B}$ , such that  $\mathbf{B} = \mathbf{RDR}^{-1}$ , and  $\mathbf{D}^{\text{a,in/out}}$  is defined in the same way as  $\mathbf{D}_{11}^{\text{a,in/out}}$ .

#### A.4. Boundary conditions used for the well-posed BVP

Since the evolution system (2.12) is incompletely parabolic (Strikwerda 1977), the corresponding BVP is well-posed if at both sides one condition is applied on the parabolic subequation and one condition is applied on each of the incoming characteristics of the hyperbolic subsystem, leaving the outgoing characteristics free from any constraint. Boundary conditions (2.14) rewrite

$$\widehat{\mathbf{U}}^{\text{a}} = \mathbf{P}^{\text{a}} \left( \widehat{\mathbf{F}}^{\text{a}} - \mathbf{N}_{\text{a}} \partial_{\xi} \widehat{\mathbf{U}}|_{\text{a}} - \widehat{X}_{\text{a}} \mathbf{S}^{\text{a},0} - \dot{\widehat{X}}_{\text{a}} \mathbf{S}^{\text{a},1} \right), \quad (\text{A } 6)$$

with  $\mathbf{P}^{\text{a}} = \mathbf{M}_{\text{a}}^{-1}$ . In order to get a well-posed BVP:

- The restriction of  $\widehat{\mathbf{U}}^{\text{a}}$  to the hyperbolic subsystem

$$\widehat{\mathbf{U}}_{\text{I}}^{\text{a}} = \mathbf{P}_{\text{I}}^{\text{a}} \left( \widehat{\mathbf{F}}^{\text{a}} - \mathbf{N}_{\text{a}} \partial_{\xi} \widehat{\mathbf{U}}|_{\text{a}} - \widehat{X}_{\text{a}} \mathbf{S}^{\text{a},0} - \dot{\widehat{X}}_{\text{a}} \mathbf{S}^{\text{a},1} \right) \quad (\text{A } 7)$$

is projected onto the incoming waves of the hyperbolic subsystem thanks to the matrix  $\mathbf{B}_{11}^{\text{a,in}}$ . Here we have used the notation  $\mathbf{P}_{\text{I}}^{\text{a}}$  that refers to the  $3 \times 4$  matrix  $(\mathbf{P}_{\text{I}}^{\text{a}})_{ij} = P_{ij}^{\text{a}}$ , for  $i = 1, \dots, 3$  and  $j = 1, \dots, 4$ .

- Heat-flux continuity (at the external surface) and total energy conservation (at the shock front) provide us with a Robin condition for the parabolic subequation

$$\mathbf{N}_{22}^{\text{a}} \partial_{\xi} \widehat{\mathbf{U}}_{\text{II}}|_{\text{a}} + \mathbf{M}_{\text{II}}^{\text{a}} \widehat{\mathbf{U}}|_{\text{a}} + \mathbf{S}_{\text{II}}^{\text{es},0} \widehat{X}_{\text{a}} + \mathbf{S}_{\text{II}}^{\text{es},1} \text{d}_t \widehat{X}_{\text{a}} = 0. \quad (\text{A } 8)$$

We have used the notation  $\mathbf{M}_{\text{II}}^{\text{a}}$  that refers to the row vector  $(\mathbf{M}_{\text{II}}^{\text{a}})_j = M_{4j}^{\text{a}}$ , for  $j = 1, \dots, 4$ . Evolution equations for the boundary deformations is given by selecting the row corresponding to velocity  $\widehat{V}_x$  in (2.14) and read

$$S_{2i}^{\text{a},1} \dot{\widehat{X}}_{\text{a}} + N_{2i}^{\text{sf}} \delta \partial_{\xi} \widehat{\mathbf{U}}_i + M_{2i}^{\text{a}} \widehat{\mathbf{U}}_i + S_{2i}^{\text{a},0} \widehat{X}_{\text{a}} = 0. \quad (\text{A } 9)$$

## Appendix B. Derivation of the adjoint problem

### B.1. Variation of the Lagrange functional

We express the variations of  $\mathcal{L}$  (3.3) with respect to the direct variables  $(\widehat{\mathbf{U}}, \widehat{X}_{\text{es}}, \widehat{X}_{\text{sf}})$  in the directions  $(\delta \widehat{\mathbf{U}}, \delta \widehat{X}_{\text{es}}, \delta \widehat{X}_{\text{sf}})$ . The main manipulations consist in replacing operators for boundary conditions and evolution equations by their expressions and performing integrations by part. The successive cancelling of the variations with respect to each of the independent variables yields the adjoint problem (3.10), (3.10), (3.11), (3.12) and (3.13). The definition of an *adjoint deformation* and an *adjoint deformation velocity* naturally stem from this derivation. Finally, we give some details about the implementation of boundary conditions for the adjoint problem.

After some integrations by part, and with the detailed expressions (A 7)-(A 9), the

expanded form of the variations of (3.3) in the directions  $(\delta\widehat{\mathbf{U}}, \delta\widehat{\mathbf{X}}_{\text{es}}, \delta\widehat{\mathbf{X}}_{\text{sf}})$  reads

$$\begin{aligned}
\delta\mathcal{L} &= \nabla_{\widehat{\mathbf{U}}|_{t_f}} \mathcal{J} \cdot \delta\widehat{\mathbf{U}}|_{t_f} + \nabla_{\widehat{\mathbf{X}}_{\text{es}}|_{t_f}} \mathcal{J} \cdot \delta\widehat{\mathbf{X}}_{\text{es}}|_{t_f} + \nabla_{\widehat{\mathbf{X}}_{\text{sf}}|_{t_f}} \mathcal{J} \cdot \delta\widehat{\mathbf{X}}_{\text{sf}}|_{t_f} \\
&+ \int_{t_0,0}^{t_f,\xi_{\text{sf}}} \left( \partial_t \widehat{\mathbf{U}}^\dagger - \mathbf{L}^\dagger \widehat{\mathbf{U}}^\dagger \right)^\top \delta\widehat{\mathbf{U}} dt d\xi - \int_0^{\xi_{\text{sf}}} \left[ \widehat{\mathbf{U}}^{\dagger\top} \delta\widehat{\mathbf{U}} \right]_{t_0}^{t_f} d\xi \\
&- \int_{t_0}^{t_f} \left[ \widehat{\mathbf{U}}^{\dagger\top} \mathbf{A} \delta \partial_\xi \widehat{\mathbf{U}} - \left( \partial_\xi (\widehat{\mathbf{U}}^{\dagger\top} \mathbf{A}) - \widehat{\mathbf{U}}^{\dagger\top} \mathbf{B} \right) \delta\widehat{\mathbf{U}} \right]_0^{\xi_{\text{sf}}} dt \\
&- \int_{t_0}^{t_f} \widehat{\mathbf{v}}_{\text{es}}^{\dagger\top} \mathbf{B}_{11}^{\text{es},\text{in}} \left[ \delta\widehat{\mathbf{U}}|_{\text{es}} - \mathbf{P}_1^{\text{es}} \left( \mathbf{I}_3 \delta\widehat{\mathbf{U}}|_{\text{es}} - \mathbf{N}^{\text{es}} \delta \partial_\xi \widehat{\mathbf{U}}|_{\text{es}} - \mathbf{S}^{\text{es},0} \delta\widehat{\mathbf{X}}_{\text{es}} - \mathbf{S}^{\text{es},1} d_t \delta\widehat{\mathbf{X}}_{\text{es}} \right) \right] dt \\
&- \int_{t_0}^{t_f} \widehat{\mathbf{v}}_{\text{sf}}^{\dagger\top} \mathbf{B}_{11}^{\text{sf},\text{in}} \left[ \delta\widehat{\mathbf{U}}|_{\text{sf}} + \mathbf{P}_1^{\text{sf}} \left( \mathbf{N}_{11}^{\text{sf}} \delta \partial_\xi \widehat{\mathbf{U}}|_{\text{sf}} + \mathbf{S}^{\text{sf},0} \delta\widehat{\mathbf{X}}_{\text{sf}} + \mathbf{S}^{\text{sf},1} d_t \delta\widehat{\mathbf{X}}_{\text{sf}} \right) \right] dt \\
&- \int_{t_0}^{t_f} \widehat{\eta}_{\text{es}}^\dagger \left( \mathbf{N}_{22}^{\text{es}} \delta \partial_\xi \widehat{\mathbf{U}}|_{\text{es}} + \mathbf{M}_{11}^{\text{es}} \delta\widehat{\mathbf{U}}|_{\text{es}} + \mathbf{S}_{11}^{\text{es},0} \delta\widehat{\mathbf{X}}_{\text{es}} + \mathbf{S}_{11}^{\text{es},1} d_t \delta\widehat{\mathbf{X}}_{\text{es}} \right) dt \\
&- \int_{t_0}^{t_f} \widehat{\eta}_{\text{sf}}^\dagger \left( \mathbf{N}_{22}^{\text{sf}} \delta \partial_\xi \widehat{\mathbf{U}}|_{\text{sf}} + \mathbf{M}_{11}^{\text{sf}} \delta\widehat{\mathbf{U}}|_{\text{sf}} + \mathbf{S}_{11}^{\text{sf},0} \delta\widehat{\mathbf{X}}_{\text{sf}} + \mathbf{S}_{11}^{\text{sf},1} d_t \delta\widehat{\mathbf{X}}_{\text{sf}} \right) dt \\
&- \int_{t_0}^{t_f} \widehat{\mu}_{\text{es}}^\dagger \left[ S_{22}^{\text{es},1} d_t \delta\widehat{\mathbf{X}}_{\text{es}} + N_{2j}^{\text{es}} \delta \partial_\xi \widehat{\mathbf{U}}_j + M_{2j}^{\text{es}} \delta\widehat{\mathbf{U}}_j + S_{22}^{\text{es},0} \delta\widehat{\mathbf{X}}_{\text{es}} \right] dt \\
&- \int_{t_0}^{t_f} \widehat{\mu}_{\text{sf}}^\dagger \left[ S_{22}^{\text{sf},1} d_t \delta\widehat{\mathbf{X}}_{\text{sf}} + N_{2j}^{\text{sf}} \delta \partial_\xi \widehat{\mathbf{U}}_j + M_{2j}^{\text{sf}} \delta\widehat{\mathbf{U}}_j + S_{22}^{\text{sf},0} \delta\widehat{\mathbf{X}}_{\text{sf}} \right] dt, \tag{B1}
\end{aligned}$$

where  $(\mathbf{I}_3)_{33} = 1$  and  $(\mathbf{I}_3)_{ij} = 0$  for  $(i, j) \neq (3, 3)$ . We have used the notation  $\mathbf{N}_{11}^{\text{a}}$  that refers to the row vector  $(\mathbf{N}_{11}^{\text{a}})_j = N_{4j}^{\text{a}}$ , for  $j = 1, \dots, 4$ .

• Cancelling variations  $\delta\widehat{\mathbf{U}}$  for all  $0 \leq \xi \leq \xi_{\text{sf}}$  and  $t_0 \leq t \leq t_f$ , yields the adjoint evolution equation

$$\begin{aligned}
\partial_t \widehat{\mathbf{U}}^\dagger &= \mathbf{L}^\dagger \widehat{\mathbf{U}}^\dagger \\
&\Leftrightarrow \partial_t \widehat{\mathbf{U}}^\dagger - \mathbf{A}^\top \partial_\xi^2 \widehat{\mathbf{U}}^\dagger + (\mathbf{B}^\top - 2 \partial_\xi \mathbf{A}^\top) \partial_\xi \widehat{\mathbf{U}}^\dagger - (\mathbf{C}^\top - \partial_\xi \mathbf{B}^\top + \partial_\xi^2 \mathbf{A}^\top) \widehat{\mathbf{U}}^\dagger = 0, \tag{B2}
\end{aligned}$$

which is equivalent to (3.10).

• Cancelling variations  $\delta\widehat{\mathbf{U}}$  at  $t_0$  and  $t_f$  yields the optimality condition (3.14b) and terminal condition (3.14a).

• Cancelling variations  $\delta\widehat{\mathbf{U}}|_{\text{es}}$  and  $\delta\widehat{\mathbf{U}}|_{\text{sf}}$  yields boundary conditions (3.11a) and (3.12a).

• Cancelling variations  $\delta \partial_\xi \widehat{\mathbf{U}}|_{\text{es}}$  and  $\delta \partial_\xi \widehat{\mathbf{U}}|_{\text{sf}}$  yields boundary conditions (3.11b) and (3.12b),

- Cancelling variations  $\delta\widehat{X}_a$  for all  $t_0 \leq t \leq t_f$  yields a scalar ODE

$$d_t \left( \widehat{\nu}_a^\dagger{}^\top \mathbf{B}_{11}^{\text{a,in}} \mathbf{P}_1^{\text{a}} \mathbf{S}^{\text{a},1} + \widehat{\eta}_a^\dagger \mathbf{S}_{\text{II}}^{\text{a},1} + \widehat{\mu}_a^\dagger \mathbf{S}_2^{\text{a},1} \right) = \widehat{\nu}_a^\dagger{}^\top \mathbf{B}_{11}^{\text{a,in}} \mathbf{P}_1^{\text{a}} \mathbf{S}^{\text{a},0} + \widehat{\eta}_a^\dagger \mathbf{S}_{\text{II}}^{\text{a},0} + \widehat{\mu}_a^\dagger \mathbf{S}_2^{\text{a},0}, \quad (\text{B } 3)$$

which defines

$$\widehat{X}_a^\dagger = \widehat{\nu}_a^\dagger{}^\top \mathbf{B}_{11}^{\text{a,in}} \mathbf{P}_1^{\text{a}} \mathbf{S}^{\text{a},1} + \widehat{\eta}_a^\dagger \mathbf{S}_{\text{II}}^{\text{a},1} + \widehat{\mu}_a^\dagger \mathbf{S}_2^{\text{a},1}, \quad (\text{B } 4)$$

and

$$\widehat{X}_a^{\dagger} = \widehat{\nu}_a^\dagger{}^\top \mathbf{B}_{11}^{\text{a,in}} \mathbf{P}_1^{\text{a}} \mathbf{S}^{\text{a},0} + \widehat{\eta}_a^\dagger \mathbf{S}_{\text{II}}^{\text{a},0} + \widehat{\mu}_a^\dagger \mathbf{S}_2^{\text{a},0}, \quad (\text{B } 5)$$

which are used in (3.13).

- Cancelling variations  $\delta\widehat{X}_a$  at  $t_0$  and  $t_f$  yields the optimality condition (3.14b) and terminal condition (3.14a).

## B.2. Implementation of the adjoint boundary conditions

As the adjoint evolution equation (3.10) has the same incompletely parabolic structure as the direct evolution equation (2.12), suitable boundary conditions have to be applied on the hyperbolic subsystem and the parabolic subequation (see § 3.2). The boundary conditions for the hyperbolic subsystem is deduced from the first three rows of (3.11a), which are decomposed into incoming and outgoing components of matrix  $\mathbf{B}_{11}^\top$ , as defined in (A 5)

$$(\mathbf{B}_{11}^{\text{in}})_{ji} \widehat{U}_1^\dagger{}_j = (\mathbf{B}_{11}^{\text{in}})_{ji} \widehat{\nu}_{\text{es}}^\dagger{}_j + \Delta_{ji}^{\text{in}} \left[ M_{j2}^{\text{es}} \widehat{\mu}_{\text{es}}^\dagger - (\mathbf{B}_{21})_i \widehat{U}_{\text{II}}^\dagger \right], \quad (\text{B } 6a)$$

$$(\mathbf{B}_{11}^{\text{out}})_{ji} \widehat{U}_1^\dagger{}_j = \Delta_{ji}^{\text{out}} \left[ M_{j2}^{\text{es}} \widehat{\mu}_{\text{es}}^\dagger - (\mathbf{B}_{21})_i \widehat{U}_{\text{II}}^\dagger \right], \quad (\text{B } 6b)$$

with

$$\Delta^{\text{in}} = [\mathbf{R}_{11} \text{diag} \{ \max\{\text{sign}(\lambda_i), 0\} \} \mathbf{R}_{11}^{-1}]^\top,$$

$$\Delta^{\text{out}} = [\mathbf{R}_{11} \text{diag} \{ \min\{\text{sign}(\lambda_i), 0\} \} \mathbf{R}_{11}^{-1}]^\top,$$

where  $\text{sign}(x) = \text{returns the sign of } x \text{ and } 0 \text{ when } x = 0$ .

As the adjoint problem is integrated backward in time, (B 6a) (respectively B 6b) corresponds to the outgoing (resp. incoming) information at the external surface.

At each integration step,  $\mathbf{B}_{11}^{\text{in}\top} \widehat{\nu}_{\text{es}}^\dagger$ ,  $\widehat{\eta}_{\text{es}}^\dagger$  and  $\widehat{\mu}_{\text{es}}^\dagger$  are unknown informations that will be determined thanks to  $\widehat{U}_{\text{es}}^\dagger|_{\text{es}}$  and  $\widehat{X}_{\text{es}}$  through the relations (B 6a), (3.11b) and the definition of  $\widehat{X}_{\text{es}}^\dagger$  (B 3). This leads to solving a  $5 \times 5$  linear system

$$\widehat{\mathbf{W}} = \mathbf{Q}\widehat{\mathbf{Z}}, \quad (\text{B } 7)$$

with

$$\widehat{\mathbf{W}} = \begin{pmatrix} (\mathbf{B}_{11}^{\text{in}})^\top \widehat{U}_1^\dagger \\ \widehat{X}_{\text{es}}^\dagger \\ \mathbf{A}_{22} \widehat{U}_{\text{II}}^\dagger \\ \mathbf{N}_{22} \widehat{U}_{\text{II}}^\dagger \end{pmatrix}, \quad \widehat{\mathbf{Z}} = \begin{pmatrix} \mathbf{B}_{11}^{\text{in}} \widehat{\nu}_{\text{es}}^\dagger \\ \widehat{\eta}_{\text{es}}^\dagger \\ \widehat{\mu}_{\text{es}}^\dagger \end{pmatrix}, \quad (\text{B } 8)$$

and the matrix  $\mathbf{Q}$  is defined by blocks which are conformal to the elements of  $\widehat{\mathbf{W}}$  and  $\widehat{\mathbf{Z}}$

$$\mathbf{Q} = \begin{pmatrix} \mathbf{Q}_{11} & \mathbf{Q}_{12} & \mathbf{Q}_{13} \\ \mathbf{Q}_{21} & \mathbf{Q}_{22} & \mathbf{Q}_{23} \\ \mathbf{Q}_{31} & \mathbf{Q}_{32} & \mathbf{Q}_{33} \end{pmatrix},$$

$$\mathbf{Q}_{11} = \text{diag}\{1, 1, 1\}, \quad \mathbf{Q}_{12} = 0, \quad (\mathbf{Q}_{13})_i = M_{2j}^{\text{es}} \Delta_{ji}^{\text{in}},$$

$$(\mathbf{Q}_{21} \quad \mathbf{Q}_{22}) = \mathbf{P}^{\text{es}} \mathbf{S}^{\text{es},1}, \quad \mathbf{Q}_{23} = S_2^{\text{es},1},$$

$$\mathbf{Q}_{31} = \mathbf{P}_{12}^{\text{es}\top}, \quad \mathbf{Q}_{32} = \mathbf{P}_{22}^{\text{es}}, \quad \mathbf{Q}_{33} = 0.$$

Once  $\mathbf{B}_{11}^{\text{in}\top} \widehat{\boldsymbol{\nu}}_{\text{es}}^\dagger$ ,  $\widehat{\boldsymbol{\eta}}_{\text{es}}^\dagger$  and  $\widehat{\boldsymbol{\mu}}_{\text{es}}^\dagger$  have been determined, the adjoint velocity deformation  $\widehat{X}_{\text{es}}$  (B3) and the right hand side of (B6b) are determined.

The Robin boundary condition for the parabolic subequations in (3.10) is taken from the fourth row of (B6b), where the right hand side depends on  $\widehat{\boldsymbol{\eta}}_{\text{es}}^\dagger$  and  $\widehat{\boldsymbol{\mu}}_{\text{es}}^\dagger$ , that have been determined above.

The same procedure applies at the shock front.

## Appendix C. Connection with a target implosion simulation

The terminal time  $t_f$  is varied in an interval whose upper bound represents the end of the shock-transit phase for an actual ICF target design. To determine this bound, we build on the results of Varillon *et al.* (2020) according to which perturbations propagate close to linear waves in the conduction and compression regions with wave speeds close to the eigenvalues of the advection matrix  $\mathbf{B}$  (2.12d). An external perturbation reaches the ablation layer as a heat-conductivity wave and then initiates a system of reflected isentropic acoustic waves and entropy waves in the compression region.

A simulation of the shock-transit phase for the chosen ICF target design (LMJ target A1040 of Saillard, 2000) with the ICF code FCI2 (Buresi *et al.* 1986) allowed us to obtain travel time estimates for a sequence of these waves going back and forth between the ablation front (af) and the shock front (sf). We then identified that over the duration of the shock-transit phase, a forward acoustic wave initially launched from the ablation front can almost accomplish the sequence of trips (af  $\rightarrow$  sf  $\rightarrow$  af  $\rightarrow$  sf  $\rightarrow$  af  $\rightarrow$  sf). From the equivalent travel times in the chosen self-similar ablation wave, the same sequence of trips is observed over the interval  $1 < t < 3.69$ : see table 7. We thus conclude that the end of the shock-transit phase for the target corresponds to a time smaller than 3.69 for the self-similar wave. Consequently, we set the upper bound on the terminal time to be  $\max t_f = 3.5$ . Over the time laps  $1 \leq t \leq 3.5$ , the self-similar ablation wave is thus equivalent, in terms of wave trips, to the shock-transit phase of the actual target.

From  $t_0$  to  $\max\{t_f\}$ , the shock front has travelled along a distance  $d_{\text{sf}}$ . We choose to conserve the dimensionless number

$$\vartheta = \frac{d_{\text{sf}}}{\max\{\lambda_\perp\}} \quad (\text{C1})$$

between the chosen ICF target design and the self-similar ablation wave. From the simulation of the ICF target implosion we get  $\vartheta = 1.4$ , and from the self-similar ablation flow (table 1)  $d_{\text{sf}} = 4.4$ , yielding the lower bound  $\min\{k_\perp\} \approx 2$ . However, ICF implosion studies explore a range of Legendre modes lower than 60, typically  $10 \leq l \leq 10^3$  (Haan *et al.* 2015, figure 3). We take this range for our study, which corresponds then to the interval  $0.33 \leq k_\perp \leq 33$ . Of course, when transposing these results to the actual geometry of a target, we must keep in mind that curvature effects may modify results for  $k_\perp < 2$ .

Wave type	Ablation layer		Shock front
Forward isentropic acoustic	1.05	→	1.28
Entropy	1.78	←	“
Forward isentropic acoustic	“	→	2.18
Entropy	3.02	←	“
Forward isentropic acoustic	“	→	3.69
Entropy	5.13	←	“

TABLE 7. Arrival times of characteristic waves at the ablation layer and shock front, from an external perturbation at  $t_0 = 1$ .

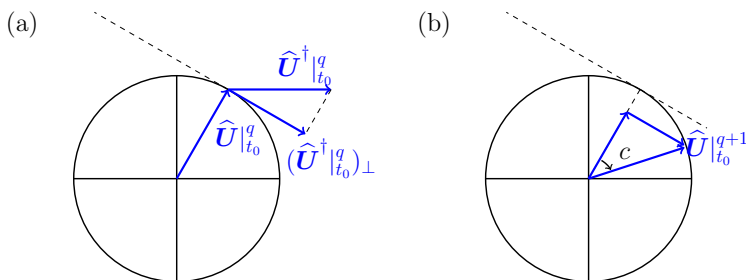


FIGURE 15. Geometrical view of the normalization (adapted from Foures *et al.*, 2013).

## Appendix D. Optimisation procedure

Once the gradient of the Lagrange functional with respect to the initial condition (3.15) has been determined at the end of the  $q$ -th iteration, a new initial condition  $(\widehat{\mathbf{U}}, \widehat{X}_{\text{es}}, \widehat{X}_{\text{sf}})|_{t_0}^{q+1}$  is computed thanks to a gradient descent

$$\widehat{\mathbf{U}}|_{t_0}^{q+1} = \widehat{\mathbf{U}}|_{t_0}^q + \epsilon \nabla_{\widehat{\mathbf{U}}|_{t_0}} \mathcal{L}, \quad (\text{D } 1a)$$

$$\widehat{X}_{\text{a}}|_{t_0}^{q+1} = \widehat{X}_{\text{a}}|_{t_0}^q + \epsilon \nabla_{\widehat{X}_{\text{a}}|_{t_0}} \mathcal{L}, \quad \text{for a = es, sf} \quad (\text{D } 1b)$$

with  $\epsilon$  the descent step. As it appears in the Lagrange functional, the unit normalization constraint is not enforced through a Lagrange multiplier. If such a method is used, the associated Lagrange multiplier would be determined such that the new initial condition would be normalized to unit, and would interfere with the choice of the descent step of the gradient method. This method proves to be very sensitive to the choice of descent step, as was observed in (Foures *et al.* 2013), and therefore we have preferred the following two methods:

- The power iteration technique amounts to choose  $\widehat{\mathbf{U}}|_{t_0}^{q+1} = \nabla_{\widehat{\mathbf{U}}|_{t_0}} \mathcal{L} = \widehat{\mathbf{U}}^\dagger|_{t_0}$  and to rescale it to unity. This method is robust but makes no use of the information contained in  $\widehat{\mathbf{U}}|_{t_0}^q$ .
- The true gradient technique proposes a geometrical interpretation of the normalization (Douglas *et al.* 2000; Foures *et al.* 2013). The initial conditions  $\widehat{\mathbf{U}}|_{t_0}$  have to belong to a unity hypersphere to comply with the normalization constraint. Hence, each new  $\widehat{\mathbf{U}}|_{t_0}^{q+1}$  is the result of the rotation of  $\widehat{\mathbf{U}}|_{t_0}^q$  by an angle  $c$  in the plane defined by  $\widehat{\mathbf{U}}|_{t_0}^q$  and

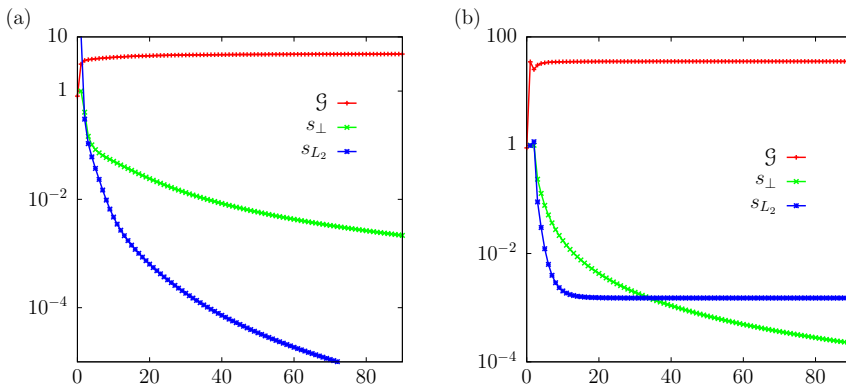


FIGURE 16. Gain curves for Chu's energy and residuals  $s_{\perp}$  (D 5) and  $s_{L_2}$  (D 4). For (a)  $r_c = 1$ ,  $(k_{\perp}, t_f) = (32, 1.1)$ , and (b)  $r_c = 0.01$ ,  $(k_{\perp}, t_f) = (1, 1.1)$ .

$\nabla_{\widehat{\mathcal{U}}|_{t_0}} \mathcal{L} = \widehat{\mathcal{U}}^{\dagger}|_{t_0}^q$  (figures 15a and b). To proceed,  $\widehat{\mathcal{U}}^{\dagger}|_{t_0}^q$  is projected onto the subspace perpendicular to  $\widehat{\mathcal{U}}|_{t_0}^q$  (figure 15a). This projection

$$(\widehat{\mathcal{U}}^{\dagger}|_{t_0}^q)_{\perp} = \widehat{\mathcal{U}}^{\dagger}|_{t_0}^q - \frac{\int_0^{\xi_{\text{sf}}} \widehat{\mathcal{U}}^{\dagger}|_{t_0}^q \widehat{\mathcal{U}}|_{t_0}^q d\xi}{\int_0^{\xi_{\text{sf}}} \|\widehat{\mathcal{U}}|_{t_0}^q\|^2 d\xi} \widehat{\mathcal{U}}|_{t_0}^q, \quad (\text{D } 2)$$

is then normalized and  $\widehat{\mathcal{U}}|_{t_0}^{q+1}$  is built as a linear combination of  $\widehat{\mathcal{U}}|_{t_0}^q$  and the normalized  $(\widehat{\mathcal{U}}^{\dagger}|_{t_0}^q)_{\perp}$ , which are orthogonal to one another (figure 15b)

$$\widehat{\mathcal{U}}|_{t_0}^{q+1} = \cos(c) \widehat{\mathcal{U}}|_{t_0}^q + \sin(c) (\widehat{\mathcal{U}}^{\dagger}|_{t_0}^q)_{\perp}, \quad \text{with } c = \frac{\|(\widehat{\mathcal{U}}^{\dagger}|_{t_0}^q)_{\perp}\|}{\|\widehat{\mathcal{U}}^{\dagger}|_{t_0}^q\|}. \quad (\text{D } 3)$$

The choice of the most adapted method to our problem is not evident. According to Kerswell *et al.* (2014; 2018), it seems that there is no alternative to confronting each method by numerical experiment. The results presented in the present article have been obtained with the power iteration method but the true gradient method has been tested and led to the same optima.

The convergence of the procedure is assessed by two residuals:

- The first one is based on the  $L_2$  norm of the difference between two subsequent initial conditions

$$s_{L_2} = \frac{\|\widehat{\mathcal{U}}|_{t_0}^q - \widehat{\mathcal{U}}|_{t_0}^{q+1}\|_{L_2}^2 + (\widehat{X}_{\text{es}}|_{t_0}^q - \widehat{X}_{\text{es}}|_{t_0}^{q+1})^2 + (\widehat{X}_{\text{sf}}|_{t_0}^q - \widehat{X}_{\text{sf}}|_{t_0}^{q+1})^2}{\|\widehat{\mathcal{U}}|_{t_0}^{q+1}\|_{L_2}^2 + (\widehat{X}_{\text{es}}|_{t_0}^{q+1})^2 + (\widehat{X}_{\text{sf}}|_{t_0}^{q+1})^2}. \quad (\text{D } 4)$$

- The second one is based on the geometrical fact that when convergence is reached the adjoint state  $\widehat{\mathcal{U}}^{\dagger}|_{t_0}$  is colinear to the OIP  $\widehat{\mathcal{U}}|_{t_0}$

$$s_{\perp} = \frac{\|(\widehat{\mathcal{U}}, \widehat{X}_{\text{es}}, \widehat{X}_{\text{sf}})|_{t_0 \perp}\|}{\|(\widehat{\mathcal{U}}, \widehat{X}_{\text{es}}, \widehat{X}_{\text{sf}})|_{t_0}\|}. \quad (\text{D } 5)$$

Convergence curves for two optimal responses are given as illustrations (figures 16). As illustrated on figure 16b,  $s_{L_2}$  is more conservative as it saturates while  $s_{\perp}$  keeps on decaying. Even for the cases where the residuals are not saturating (figure 16a), the

decay quickly slows down after a few iterations. To improve the convergence speed, a more sophisticated descent algorithm could be useful, such as conjugate gradient. The true gradient method is well adapted to such a perspective, as the line maximization — which is the difficulty of conjugate gradient — is performed directly on the scalar  $c$ , with a search interval that is furthermore restricted, by the definition of  $c$ , to  $[0, \pi]$ .

## REFERENCES

- ABÉGUILÉ, F., BOUDESOCQUE-DUBOIS, C., CLARISSE, J.-M., GAUTHIER, S. & SAILLARD, Y. 2006 Linear perturbation amplification in self-similar ablation flows of inertial confinement fusion. *Phys. Rev. Lett.* **97**, 035002.
- AGLITSKIY, Y. & OTHERS 2010 Basic hydrodynamics of Richtmyer–Meshkov-type growth and oscillations in the inertial confinement fusion-relevant conditions. *Phil. Trans. R. Soc. A* **368**, 1739–1768.
- ALI, S. J. & OTHERS 2018 Probing the seeding of hydrodynamic instabilities from nonuniformities in ablator materials using 2D velocimetry **25** (9), 092708.
- ATZENI, S. & MEYER-TER-VEHN, J. 2004 *The physics of inertial fusion*. Oxford, U.K.: Oxford University Press.
- BODNER, S. E. 1974 Rayleigh–Taylor instability and laser-pellet fusion. *Phys. Rev. Lett.* **33** (13), 761–764.
- BOUDESOCQUE-DUBOIS, C. 2000 Perturbations linéaires d’une solution autosemblable de l’hydrodynamique avec conduction non linéaire. Thèse de doctorat, Université de Paris 6.
- BOUDESOCQUE-DUBOIS, C., CLARISSE, J.-M. & GAUTHIER, S. 2003 A spectral Chebyshev method for linear stability analysis of one-dimensional exact solutions of gas dynamics. *J. Comput. Phys.* **184**, 592–618.
- BOUDESOCQUE-DUBOIS, C., GAUTHIER, S. & CLARISSE, J.-M. 2008 Self-similar solutions of unsteady ablation flows in inertial confinement fusion. *J. Fluid Mech.* **603**, 151–178.
- BOUDESOCQUE-DUBOIS, C., GAUTHIER, S., CLARISSE, J.-M. & LOMBARD, V. 2006 Self-similar solutions of unsteady ablation flow. In *33rd EPS Conference on Plasma Physics, Europhysics Conference Abstracts*, vol. 301, pp. P–1.006. EPS, (CD-ROM).
- BOUDESOCQUE-DUBOIS, C., LOMBARD, V., GAUTHIER, S. & CLARISSE, J.-M. 2013 An adaptive multidomain Chebyshev method for nonlinear eigenvalue problems: Application to self-similar solutions of gas dynamics equations with nonlinear heat conduction. *J. Comput. Phys.* **235**, 723–741.
- BURESI, E. & OTHERS 1986 Laser program development at CEL-V: overview of recent experimental results. *Laser Part. Beams* **4**, 531.
- CHANDRASEKHAR, S. 1961 *Hydrodynamic and hydromagnetic stability*. Oxford University Press.
- CHU, B.-T. 1965 On the energy transfer to small disturbances in fluid flow (part I). *Acta Mechanica* **1**, 215–234.
- CLARISSE, J.-M., BOUDESOCQUE-DUBOIS, C. & GAUTHIER, S. 2008 Linear perturbation response of self-similar ablative flows relevant to inertial confinement fusion. *J. Fluid Mech.* **609**, 1–48.
- CLARISSE, J.-M., GAUTHIER, S., DASTUGUE, L., VALLET, A. & SCHNEIDER, N. 2016 Transient effects in unstable ablation fronts and mixing layers in HEDP. *Phys. Scr.* **91**, 074005.
- CLARISSE, J.-M., PFISTER, J.-L., GAUTHIER, S. & BOUDESOCQUE-DUBOIS, C. 2018 A hydrodynamic analysis of self-similar radiative ablation flows. *J. Fluid Mech.* **848**, 219–255.
- CLARK, D. S. & OTHERS 2019 Three-dimensional modeling and hydrodynamic scaling of national ignition facility implosions. *Physics of Plasmas* **26** (5), 050601.
- DOUGLAS, S. C., AMARI, S. & KUNG, S.-Y. 2000 On gradient adaptation with unit-norm constraints **48** (6), 1843–1847.
- FOURES, D. P. G., CAULFIELD, C. P. & SCHMID, P. J. 2012 Variational framework for flow optimization using seminorm constraints. *Phys. Rev. E* **86** (2), 026306.
- FOURES, D. P. G., CAULFIELD, C. P. & SCHMID, P. J. 2013 Localization of flow structures using  $\infty$ -norm optimization. *J. Fluid Mech.* **729**, 672–701.
- GAUTHIER, S., LE CREURER, B., ABÉGUILÉ, F., BOUDESOCQUE-DUBOIS, C. & CLARISSE, J.-

- M. 2005 A self-adaptive domain decomposition method with Chebyshev method. *Int. J. Pure Appl. Math.* **24**, 553–577.
- GILES, M.B. & PIERCE, N.A. 1997 Adjoint equations in cfd - duality, boundary conditions and solution behaviour. In *13th Computational Fluid Dynamics Conference*.
- GILES, M.B. & PIERCE, N.A. 2000 An introduction to the adjoint approach to design. *Flow Turb. Combust.* **65**, 393–415.
- GONCHAROV, V. N. 1999 Theory of the ablative Richtmyer-Meshkov instability. *Phys. Rev. Lett.* **82** (10), 2091–2094.
- GONCHAROV, V. N., BETTI, R. & MCCRORY, R. L. 1996 Self-consistent stability analysis of ablation fronts with small Froude numbers. *Phys. Plasmas* **3** (12), 4665–4676.
- GONCHAROV, V. N., SKUPSKY, S., BOEHLY, T. R., KNAUER, J. P., MCKENTY, P., SMALYUK, V. A., TOWN, R. P., GOTCHEV, O. V., BETTI, R. & MEYERHOFER, D. D. 2000 A model of laser imprinting. *Phys. Plasmas* **7** (5), 2062–2068.
- GONCHAROV, V. N. & OTHERS 2006 Early stage of implosion in inertial confinement fusion: Shock timing and perturbation evolution. *Phys. Plasmas* **13**, 012702.
- GUÉGAN, A., SCHMID, P. J. & HUERRE, P. 2006 Optimal energy growth and optimal control in swept Hiemenz flow. *J. Fluid Mech.* **566**, 11–45.
- GUNZBURGER, M. D. 1997 Introduction into mathematical aspect of flow control and optimization. In *Lecture Series 1997-05 on Inverse Design and Optimisation Methods* (ed. von Karman Institute for Fluid Dynamics).
- HAAN, S. W., HUANG, H., JOHNSON, M. A., STADERMANN, M., BAXAMUSA, S., BHANDARKAR, S., CLARK, D. S., SMALYUK, V. & ROBNEY, H. F. 2015 Instability growth seeded by oxygen in CH shells on the National Ignition Facility. *Phys. Plasmas* **22** (3), 032708.
- HAINES, BRIAN M. & OTHERS 2019 Robustness to hydrodynamic instabilities in indirectly driven layered capsule implosions. *Physics of Plasmas* **26** (1), 012707.
- HIRSCH, C. 1988 *Numerical computation of internal and external flows*. Chichester: Wiley.
- HUETE, C., WOUCHUK, J. G., CANAUD, B. & VELIKOVICH, A. L. 2012 Analytical linear theory for the shock and re-shock density inhomogeneities. *J. Fluid Mech.* **700**, 214–245.
- KERSWELL, R. R. 2018 Nonlinear nonmodal stability theory. *Annu. Rev. Fluid Mech.* pp. 319–346.
- KERSWELL, R. R. & OTHERS 2014 An optimization approach for analysing nonlinear stability with transition to turbulence in fluids as an exemplar. *Reports on Progress in Physics* **77**.
- KOVÁSZNAY, L. S. G. 1953 Turbulence in supersonic flow. *J. Aeronautic. Sci.* **20** (10), 657–674.
- KREISS, H.-O. 1970 Initial boundary value problems for hyperbolic systems. *Commun. Pure Appl. Math.* **23**, 277–298.
- KULL, H. J. 1989 Incompressible description of Rayleigh–Taylor instabilities in laser-ablated plasmas. *Phys. Fluids B* **1**, 170–182.
- KULL, H. J. & ANISIMOV, S. I. 1986 Ablative stabilization in the incompressible Rayleigh–Taylor instability. *Phys. Fluids* **29**, 2067–2075.
- LEMKE, M., REISS, J. & SESTERHENN, J. 2014 Compressible flow, reactive flow, adjoint equations. *Combust. Flame* **161** (10), 2552–2564.
- LINDL, J. 1995 Development of the indirect-drive approach to inertial confinement fusion and the target physics basis for ignition and gain. *Phys. Plasmas* **2** (11), 3933–4024.
- LINDL, J., AMENDT, P., BERGER, R., GLENDINNING, S., GLENZER, S., HAAN, S., KAUFFMAN, R., LANDEN, O. & SUTER, L. 2004 The physics basis for ignition using indirect-drive targets on the National Ignition Facility. *Phys. Plasmas* **11** (2), 339–491.
- LINDL, J., LANDEN, O., EDWARDS, J., MOSES, E. & NIC TEAM 2014 Review of the National Ignition Campaign 2009–2012. *Phys. Plasmas* **21**, 020501.
- LOMBARD, V., GAUTHIER, S., CLARISSE, J.-M. & BOUESOCQUE-DUBOIS, C. 2008 Kováznay modes in stability of self-similar ablation flows of ICF. *Europhys. Lett.* **84**, 25001.
- LUCHINI, P. & BOTTARO, A. 1998 Gortler vortices: a backward-in-time approach to the receptivity problem. *J. Fluid Mech.* **363**, 47–65.
- LUCHINI, P. & BOTTARO, A. 2014 Adjoint equations in stability analysis. *Annu. Rev. Fluid Mech.* **46** (1), 493–517.
- MARSHAK, R. 1958 Effect of radiation on shock wave behavior. *Phys. Fluids* **1** (1), 24–29.
- MIHALAS, D. & MIHALAS, B. W. 1984 *Foundations of radiation hydrodynamics*. Oxford: Oxford University Press.

- NICOUD, F., BENOIT, L., SENSAIU, C. & POINSOT, T. 2007 Acoustic modes in combustors with complex impedances and multidimensional active flames. *AIAA Journal, American Institute of Aeronautics and Astronautics* **45** (2), 426–441.
- PAKULA, R. & SIGEL, R. 1985 Self-similar expansion of dense matter due to heat transfer by nonlinear conduction. *Phys. Fluids* **28**, 232–244.
- PETERSON, J. L., CASEY, D. T., HURRICANE, O. A., RAMAN, K. S., ROBNEY, H. F. & SMALYUK, V. A. 2015 Validating hydrodynamic growth in National Ignition Facility implosions. *Physics of Plasmas* **22** (5), 056309.
- RAMAN, K. S. & OTHERS 2014 An in-flight radiography platform to measure hydrodynamic instability growth in inertial confinement fusion capsules at the National Ignition Facility. *Phys. Plasmas* **21**, 072710.
- REINICKE, P. & MEYER-TER-VEHN, J. 1991 The point explosion with heat conduction. *Phys. Fluids A* **3**, 1807–1818.
- SANZ, J. 1996 Self-consistent analytical model of the Rayleigh–Taylor instability in inertial confinement fusion. *Phys. Rev. E* **53** (4), 4026–4045.
- SCHMID, P. J. & HENNINGSON, D. S. 2001 *Stability and transition in shear flows*. Springer.
- SMALYUK, V. A. & OTHERS 2015 Hydrodynamic instability growth of three-dimensional, native-roughness modulations in x-ray driven, spherical implosions at the National Ignition Facility. *Phys. Plasmas* **22**, 072704.
- SMALYUK, V. A. & OTHERS 2017 Hydrodynamic instability growth of three-dimensional modulations in radiation-driven implosions with low-foot and high-foot drives at the National Ignition Facility. *Phys. Plasmas* **24**, 042706.
- STRIKWERDA, J. C. 1977 Initial boundary value problems for incompletely parabolic systems. *Commun. Pure Appl. Math.* **30** (6), 797–822.
- TOMMASINI, RICCARDO & OTHERS 2020 Time-resolved fuel density profiles of the stagnation phase of indirect-drive inertial confinement implosions. *Phys. Rev. Lett.* **125**, 155003.
- VARILLON, G. 2019 Nonmodal hydrodynamic stability analysis of ablation flows relative to inertial confinement fusion. Thèse de doctorat, Université Paris-Saclay, École polytechnique.
- VARILLON, G., CLARISSE, J.-M. & COUAIRO, A. 2020 Investigation of supersonic heat-conductivity hyperbolic waves in radiative ablation flows. *Phys. Rev. E* **101**, 043215.
- VARILLON, G., CLARISSE, J.-M. & COUAIRO, A. 2021 Stability of ablation flows in inertial confinement fusion: Nonmodal effects. *Phys. Rev. E* **In press**.
- VELIKOVICH, A. L., DAHLBURG, J. P., GARDNER, J. H. & TAYLOR, R. J. 1998 Saturation of perturbation growth in ablatively driven planar laser targets. *Phys. Plasmas* **5**, 1491–1505.
- VOLKOV, O., PROTAS, B., LIAO, W. & GLANDER, D. W. 2009 Adjoint-based optimization of thermo-fluid phenomena in welding processes. *J. Eng. Math.* **65**, 201220.
- WIECZOREK, K. & OTHERS 2011 Assessing non-normal effects in thermoacoustic systems with mean flow. *Phys. Fluids* **23** (10), 107103.
- ZEL'DOVICH, YA. B. & RAIZER, YU. P. 1967 *Physics of shock waves and high-temperature hydrodynamic phenomena*. New-York: Academic Press.